THESIS

MANTLE VELOCITY VARIATIONS UNDER THE NORTHERN CANADIAN CORDILLERA THROUGH BODY WAVE TOMOGRAPHY

Submitted by

Aditya U. Khare

Department of Geosciences

In partial fulfillment of the requirements

For the Degree of Master of Science

Colorado State University

Fort Collins, Colorado

Fall 2019

Master's Committee:

Advisor: Derek Schutt

Kristen Buchanan
Sven Egenhoff

ABSTRACT

MANTLE VELOCITY VARIATIONS UNDER THE NORTHERN CANADIAN CORDILLERA THROUGH BODY WAVE TOMOGRAPHY

The Mackenzie Mountains (MM) in the northern Canadian Cordillera (NCC) are an actively uplifting mountain range and an excellent location to investigate the causes of intra-plate orogeny. The orogen is situated almost $\sim$750 km inboard of the active Pacific plate boundary, and little deformation is occurring between the MM and the Pacific Coast, except within the Coast Ranges. To investigate the causes of this orogeny, the Mackenzie Mountains Earthscope Project (MMEP) deployed 40 broadband seismographs and 4 continuous GPS instruments in a linear array from near the Pacific Coast to the Slave craton. Here we present results of teleseismic body wave tomography in the NCC that were obtained by using data from 37 of these MM stations as well as 67 other stations in the region surrounding the MM. Results show a sharp sub-vertical transition between low velocity in the Cordillera (ΔV -2%) and high velocity in the craton (ΔV +2%) about 100 km southwest of the Mackenzie River. The locations of Miocene to Present volcanism in the region also coincide well with the low velocity zones suggesting the presence of melt and/or anomalous temperatures. Two notable high velocity anomalies are seen beneath the Cordillera. The first is present under the Tintina Fault (ΔV +1.5%) and may be indicative of a lower crustal compositional anomaly. The other is at 600 km depth below the Cordillera (ΔV_p +2%) which we interpret as delaminated lithosphere. The delamination possibly resulted from mantle upwelling due to the opening of the slab window $\sim$20 Ma.

ACKNOWLEDGEMENTS

I would like to thank my advisor Dr. Derek Schutt for his invaluable support and guidance throughout my educational journey here at CSU. I would also like to thank all the faculty members at the department of Geosciences at CSU for teaching such intellectually stimulating courses and also for giving me the opportunity to be a Teaching Assistant. A big thank you to my family for their love and support (both emotional and financial). Lastly, special thanks to Dr. Nick Rawlinson, the writer of the "Fast Marching" code used in this study, for his guidance on its execution.

TABLE OF CONTENTS

ABSTRACT ii
ACKNOWLEDGEMENTS iii
LIST OF FIGURES v

Chapter 1 1
1.1 Introduction 1
1.2 Body Wave Tomography 1
1.2.1 Bandpassing 3
1.2.2 Multi-channel Cross Correlation 4
1.2.3 Calculation of Travel Time Residuals 4
1.2.4 The Inversion Scheme 6

Chapter 2 9
2.1 Introduction 9
2.2 Data and Method 12
2.3 Results 14
2.3.1 P wave results 14
2.3.1.1 Perturbations with respect to AK135 14
2.3.2 S wave results 15
2.3.2.1 Perturbations with respect to AK135 15
2.3.3 Resolution Tests 15
2.3.3.1 P waves 15
2.3.3.2 S waves 16
2.4 Discussion 16
2.5 Conclusions 19

Chapter 3 20
3.1 Future Work 20
3.2 Data Processing Sequence 21

Chapter 4 27
4.1 Figures 27

References 47

LIST OF FIGURES

4.1 A record section showing the arrival of different phases at stations in the NCC 27
4.2 Example results from other tomography studies 27
4.3 Effect of bandpassing on a seismogram 28
4.4 Spectra of traces before and after bandpassing 28
4.5 Cross correlated traces 29
4.6 A 2x2 grid scheme for tomography 29
4.7 Tectonic setting of the NCC 30
4.8 Station locations in the NCC 31
4.9 Slab window under the western North America 32
4.10 Backazimuthal distribution of events used in this study 32
4.11 Plots of P wave residuals 33
4.12 Histogram of P wave residuals 33
4.13 V_p trade off curve for AK135 as a starting model 34
4.14 Depth slices showing V_p perturbations with respect to AK135 35
4.15 Cross section along the MM transect showing V_p perturbations with respect to AK135. 36
4.16 Depth slices showing Vp checkerboard results 37
4.17 Vp checkerboard results along the MM array 38
4.18 Vp checkerboard results along an EW cross section 38
4.19 Histogram of V_s residuals and V_s elbow curve for AK135 as the starting model 39
4.20 Plot of mean V_s residual at each station 39
4.21 Depth slices showing V_s checkerboard results 40
4.22 V_s checkerboard results along the MM array 41
4.23 V_s checkerboard results along an EW cross section 42
4.24 Depth slices showing V_s perturbations with respect to AK135 43
4.25 Cross section along the MM transect showing V_s perturbations with respect to AK135. 44
4.26 Map of the different morphologic belts in the NCC 45
4.27 Body wave tomography results of (Mercier et al. [2009]) 45
4.28 Lithospheric strength profiles from Hyndman et al. [2005] 46

Chapter 1

1.1 Introduction

This Master's thesis is composed of three chapters. Chapter 1 lays out the background of this project which includes information on tomography, and signal processing. Chapter 2 is written in a more technical language and will be submitted to a peer-reviewed journal. Chapter 3 presents ideas for future work and also provides details of the specific steps taken in terms of data processing and tomographic inversion in this project. The goal of this chapter is to ensure that the results presented in this thesis can be reproduced at a later time.

1.2 Body Wave Tomography

Studying seismic velocities is a common practice in the realm of Seismology/Geophysics. Mantle velocities convey useful information regarding temperature variations, and thus the strength of the rock. Velocity models can also shed light on the tectonic history of the region.

The technique of imaging the deep earth using seismic velocities is called "tomography" and has two different types: 1) local tomography and 2) teleseismic tomography. This project is the latter, where the seismic sources generating the energy are not inside the model region containing the receivers and (could) lie thousands of kilometers away. The principle is simple. In the event of an earthquake, seismic waves propagate in all directions from the epicenter at some average velocity. When a portion of a wavefront passes through a relatively hot region, its velocity decreases, while when it passes through a relatively cold region, its velocity increases. These changes in velocity affect the total travel time of that wavefront from the epicenter to the station at which it is recorded. The travel time t for a wavefront along its ray path l is:

$$t = \int_{source}^{receiver} s(\mathbf{x}(l))dl \tag{1.1}$$

where s(**x**) is the slowness (reciprocal of velocity) along the ray path at a point **x**, and *dl* is an infinitesimally small segment along the ray path.

The first step of the analysis is to observe the traces (synonym for “seismograms") and calculate the relative difference between the actual and predicted arrival times for a phase of interest (Figure 4.1). These differences are called “travel time residuals" and are used to invert for the velocity model.

The inverse problem is non-unique because a wide range of velocity models can satisfy the dataset of these residuals equally well. To ensure that a model is obtained that best reflects the crustal and mantle structure of the study region, we start with a known velocity model from previous studies. If little or no information is available on the velocity structure of the region, we can use simple radially-averaged 1D models such as “PREM" (Dziewonski and Anderson [1981]) or “AK135" (Kennett et al. [1985]). The goal is to invert the aforementioned residuals to get an updated velocity model which is different from the input model since it attempts to explain the residuals. We then calculate the “perturbations" or the difference between the inverted model and the input model. In most cases, these perturbations are are of the order of a few percent or less.

Typically, the negative perturbations are shown in red, positive perturbations in blue, and 0% perturbations in white. This is because the negative perturbations (or velocities lower than those in the starting model) are generally thought to be a result of relatively higher temperatures, and positive perturbations (or velocities higher than those in the starting model) are typically a result of lower temperatures. However, other possible causes of mantle velocity variations are changes in composition, the presence of melt, and attenuation. Compositional changes are the primary reason for velocity variations in the crust while temperature changes cause velocity variations in the mantle. Calculating the ratio between P wave and S wave velocities can also provide clues to the cause of velocity variations. For example, V_p and V_s reductions per percent partial melt are at least 3.6% and 7.9%, respectively (Hammond and Humphreys [2000]). In other words, the reduction in V_s because of melt is more than that in V_p. Similarly, anelasticity, which refers to heating of the propagation medium at the expense of the energy in seismic wave resulting in

its decay, can also reduce seismic velocities. Anelasticity studies suggest that the near-solidus temperature anomalies associated with low velocity zones in the model are significantly smaller, and the amplitude of these low velocity anomalies are significantly larger for S waves than for P waves (Karato [1993]). For example, using the temperature derivatives of V_p from Karato [1993], in a non-attenuating medium (quality factor Q = ∞), a 1% V_p anomaly would map to a temperature anomaly (ΔT) of 161.3 K. However, the same V_p anomaly in a more attenuating medium, say Q = 50, would map to a temperature anomaly of (ΔT) 46 K.

Some common tectonic features that get highlighted in tomography results are stable cratons (these are lower in temperature, and show up as blue high velocity anomalies), volcanic centers (high temperatures/melt which create low velocities, and appear red), subducting oceanic slabs (high velocities, appear blue) etc. Some of these features are shown in Figure 4.2. Therefore, it is a very useful technique to study the deformation, and compositional and thermal structure of crust and upper mantle.

The processing steps in a teleseismic tomography project such as this one are listed in Chapter 3. Four of the most important steps, however, are bandpassing, multi-channel cross correlation, calculating the travel time residuals, and the final tomographic inversion. These will be discussed in some detail presently.

1.2.1 Bandpassing

Bandpassing refers to applying a filter to a seismogram so that frequencies outside the range of the filter are suppressed, noise is minimized and the arrival of a phase of interest becomes easier to observe (Figure 4.3). Depending on the phase of interest, a frequency range is determined (0.1 Hz - 2.0 Hz for P waves and 0.05 Hz - 0.4 Hz for S waves was used for this project). Because teleseismic P waves and S waves typically have frequencies 1 Hz and 0.08 Hz respectively, these filters bring out the arrivals of these phases in seismograms.

Another way to visualize this process is to take the Fourier transform of the raw trace and that of the same trace after bandpassing. While a seismogram is in the time domain, its Fourier transform

is in the frequency domain and shows the frequencies that constitute that particular seismogram. A spectrum of the raw trace at station MM05 from Figure 4.3a is shown in Figure 4.4a while that of the same trace after bandpassing is in Figure 4.4b. These spectra have the frequency content on the x-axis and the amplitudes on the y-axis. Note that the range of the filter was 0.1 Hz - 2.0 Hz.

1.2.2 Multi-channel Cross Correlation

The second step is to determine which events have a strong consistent signal across the model region. The similarity between these seismograms is measured using cross-correlation. For each event, the seismograms are aligned on top of each other with respect to the observed arrival of the phase of interest, and each trace is cross correlated with the others to calculate a normalized coefficient which can range from -1 to 1 (Figure 4.5). The more positive this coefficient, the more similar the traces are. If the coefficient is higher than a pre-defined threshold, the traces are accepted as good. This process is carried out for every possible pair of traces for all the bandpassed events, and events identified as high quality are selected for further processing (these events will hereon be referred to as “good events").

1.2.3 Calculation of Travel Time Residuals

The third step is calculating the travel time residuals from the traces of these good events. To do this, we use the method of multi-channel cross-correlation coupled with least squares (VanDecar and Crosson [1990]). This automated method provides more accurate residuals as well as uncertainties, the latter of which are crucial in the convergence of tomographic inversions. The basic approach of this method is this: 1) calculate the time difference (also known as the delay time) between the arrival of a phase in two traces by cross-correlating the traces, calculating the cross-correlation coefficient at every offset, and noting the offset (“lag time") at which this coefficient is maximized, and 2) calculate optimized arrival time (also referred to as the “actual arrival time”) of that phase in each trace using the least-squares method.

Here are those steps in more detail:

Step 1:

For an event that was recorded at, say, 3 stations (and hence has 3 traces), we perform cross-correlation between each possible pair of traces, note the lag time which gives the maximum value of the cross-correlation function between each pair, and use it to calculate the "cross-correlation derived relative delay time" between the *i*th and the *j*th traces. For this example, we will have Δt_{12}, Δt_{13}, and Δt_{23} where Δt_{ij} is the delay time of a phase between the *i*th and *j*th trace.

Step 2:

We now calculate the optimized arrival time (also known as "actual arrival time") of the phase in each of the three traces using least-squares. For *n* stations, we can set up *n*(*n*-1)/2 linear equations as follows:

$$t_i - t_j = \Delta t_{ij} \tag{1.2}$$

where t_i and t_j are the actual arrival times of that phase in traces *i* and *j* respectively, and Δt_{ij} is the delay time calculated above.

Also note that $\Delta t_{13} = \Delta t_{12} + \Delta t_{23}$. But Δt_{13} is also equal to $t_1 - t_3$.

To this system of equations we add the following constraint to force the mean of the resulting optimized arrival times to zero:

$$\sum_{i=1}^{n} t_i = 0 \tag{1.3}$$

For this example with 3 stations, we will solve four equations. We set up these equations as $\mathbf{A}t = \Delta t$ where *t* is the solution vector of optimized arrival times we have to solve for, Δt is a vector of "cross-correlation derived relative delay times", and **A** is a sparse coefficient matrix. Solving this system, specified as follows, yields the 3 equations implicit in expression (1.2), and also imposes the constraint from expression (1.3)

$$\begin{bmatrix} 1 & -1 & 0 \\ 0 & 1 & -1 \\ 1 & 0 & -1 \\ 1 & 1 & 1 \end{bmatrix} \begin{bmatrix} t_1 \\ t_2 \\ t_3 \end{bmatrix} = \begin{bmatrix} \Delta t_{12} \\ \Delta t_{23} \\ \Delta t_{13} \\ 0 \end{bmatrix}.$$

We solve this system of equations using least squares as:

$$\mathbf{t} = (\mathbf{A}^T\mathbf{A})^{-1}\mathbf{A}^T\Delta\mathbf{t} \tag{1.4}$$

Once we have the optimized arrival times, **t**, we can calculate the relative travel time residuals by removing the mean of the predicted arrival times, and subtracting them from these zero-mean optimized arrival times.

Figure 4.5 shows cross correlated traces and the calculated travel time residuals for each trace of an event recorded at seismic stations in the NCC (station names are along the left margin). For stations in the Cordillera (MM15, MM23 etc.), the actual arrival is later than predicted, while for the cratonic stations (e.g. MM38 and MM40) the arrival is earlier than predicted. However, because the script uses the formula "*predicted arrival time - actual arrival time*", the signs of the residuals are opposite of what they should be. As a result, for this project, the sign of each residual was changed before carrying out the inversion.

1.2.4 The Inversion Scheme

The fourth and final step, tomographic inversion, is the process of solving for a velocity model given a dataset of the relative travel time residuals. Because a variety of different models can satisfy the data, it is important to find the most realistic model. In addition to our geologic knowledge of the area, a few more aspects help to ensure this: a) a large number of accurately calculated residuals and uncertainties b) a good number of events with comprehensive backazimuthal distribution (events arriving at the seismic array from all four directions), and c) a starting velocity model that incorporates some information derived from previous studies. When no information about the

model region in question is available, one can use one of the radially-averaged 1D models PREM (Dziewonski and Anderson [1981]) or AK135 (Kennett et al. [1985]) as the starting model.

As a demonstration of the mathematics, consider a 2-D ray tracing tomography example where a 2x2 grid is traversed by six rays (Figure 4.6). Also assume that the length of the side of each square is 1. Usually in teleseismic tomography there are both well-resolved and unresolved model parameters. This means that at some places in the model the velocity anomalies are well constrained because of a comprehensive ray coverage while in others they are not.

To solve the inverse problem of calculating the slowness, we set up the equation $\mathbf{G}\vec{m}=\vec{d}$ as:

$$\begin{bmatrix} 1 & 0 & 1 & 0 \\ 0 & 1 & 0 & 1 \\ 0 & \sqrt{2} & \sqrt{2} & 0 \\ \sqrt{2} & 0 & 0 & \sqrt{2} \\ 1 & 1 & 0 & 0 \\ 0 & 0 & 1 & 1 \end{bmatrix} \begin{bmatrix} s_1 \\ s_2 \\ s_3 \\ s_4 \end{bmatrix} = \begin{bmatrix} t_1 \\ t_2 \\ t_3 \\ t_4 \\ t_5 \\ t_6 \end{bmatrix}$$

G is a 6x4 matrix where elements in each row represent the lengths of the six rays in each box that they pass through, $\vec{m}$ is a 4x1 vector containing the unknown slowness values of each block, and $\vec{d}$ is a 6x1 data vector containing the total travel time for each ray path. Solving this system yields one travel time equation (expression 1.1 above) for each ray. For example, ray 1 travels through boxes 1 and 3 only and hence has the travel time equation:

$$s_1 + s_3 = t_1$$

In inverse problems, the goal is to find the most realistic model that minimizes the misfit between the predicted data ($\mathbf{G}\vec{m}$) and actual data $\vec{d}$. The "residual" vector is $\mathbf{G}\vec{m}-\vec{d}$ and its magnitude that needs to be minimized is $\|\mathbf{G}\vec{m}-\vec{d}\|_2$. To achieve this and also to address the issue of solution non-uniqueness, we use a "damped least squares" solution

$$min\|\mathbf{G}\vec{m}-\vec{d}\|_2^2+\alpha^2\|\vec{m}\|_2^2 \tag{1.5}$$

where α is the *damping factor*, also called a regularization parameter (Aster et al. [2011]).

As α is increased, the perturbations from the starting model become smaller, but the data misfit increases. For example, a very high damping value would reduce the perturbations to be near zero and the resulting model will essentially be the input model. Conversely, lower α values increase the fit to the data but at the cost of high model norm $\|\vec{m}\|_2$ which implies bigger perturbations that are geologically unrealistic. Hence, we solve the problem with different values of α and plot the resulting fit to the data against the model norm which results in an L-shaped curve, called a "trade-off curve". The damping value at the corner of this curve is one way to balance the competing factors of good fit to the data and low model norm, and hence the model obtained with this damping is often considered the best solution, although the choice of damping is subjective. However, note that such a model might still not be geologically plausible.

Lastly, it is important to mention the advantages of using the Fast Marching Method (FMM) (Sethian [1996]) used in this project over the traditional ray tracing methods of tomography. There are two types of traditional ray tracing: the shooting method and the bending method. The shooting method is based on the initial value problem where a ray is specified by its initial point and its initial direction at that point (Nolet [1987]). The problem of solving for the ray path is therefore an inverse problem where the initial direction vector of the ray is the unknown, and the function to be minimized is a measure of the distance between the ray end point and the receiver (e.g. Rawlinson et al. [2007]). In the bending method, the geometry of an initial arbitrary ray path joining the source and the receiver is iteratively adjusted till it satisfies Fermat's principle and becomes the true ray path (e.g. Rawlinson and Sambridge [2005]; Rawlinson et al. [2007]).

The advantages of the FMM (Sethian [1996]) over traditional ray tracing method are as follows (Rawlinson and Sambridge [2005]): 1) It is more robust in the presence of small scale velocity variations, 2) it is faster than the ray tracing algorithms and hence useful for problems involving a large number of sources and ray paths, 3) it converges to the ray path of the first arrival (global minimum of the travel time) from source to receiver, and 4) it can also track multiple reflections within one layer.

Chapter 2

2.1 Introduction

The northern Canadian Cordillera (NCC) has a complex tectonic history. Broadly speaking, to the west of the dextral Tintina fault the Cordillera is comprised of accreted terranes that were sutured to the North American continental margin between Early Mesozoic to Early Cenozoic (e.g. Monger and Price [2002]; Nelson et al. [2013]). To the east, a series of mountain ranges lie on Precambrian basement and are capped with sediments showing a cratonic affinity (Nelson et al. [2013]). For the purposes of this study, it will be considered that the NCC is bounded to the west by the active Pacific plate boundary, to the east by the Rocky Mountain Deformation Front, to the north by the Beaufort Sea, and to the south (roughly) by the Liard Transfer Zone (LTZ) (Figure 4.7). The LTZ is an important lithospheric structural transition oriented northeast-southwest inherited from the asymmetric rifted margin of Laurentia in the Late Proterozoic (Hansen et al. [1993]; Cecile et al. [1997]). The Mackenzie Mountains (MM) are a prominent actively-uplifting arcuate salient of the NCC situated $\sim$750 km inboard of the Pacific plate boundary. Deformation of the MM initially started in the middle-Cretaceous to Paleocene (Gordey et al. [2011]; Powell et al. [2016]), and reactivated $\sim$30 Ma (Enkelmann et al. [2019]). Active seismicity associated with NE-SW directed shortening indicates a modern phase of uplift (Leonard et al. [2008]); however, the mechanisms causing the current episode of deformation and seismicity in the MM are debated (Mazzotti and Hyndman [2002]; Finzel et al. [2015]).

Current deformation in the western NCC is related to northwest-oriented oblique subduction of a small composite oceanic-continental terrane called the Yakutat Indentor under southern Alaska (Mazzotti and Hyndman [2002]). Thermochronology suggests that subduction initiated sometime between 35-10 Ma (e.g. Plafker et al. [1994]; Enkelmann et al. [2019]). Yakutat convergence has caused intense seismicity and mountain building within the Chugach and St. Elias Mountains near the coast (Page et al. [1991]). In the central Cordillera, northeast from the collision zone, little deformation is occurring. However, two major lithospheric-scale dextral faults, the Denali and

Tintina Faults, may indicate significant lithospheric boundaries (e.g. Gabrielse et al. [2006]) (Figure 4.7), although currently they exhibit relatively low slip rates (<1 mm/yr) and limited seismicity (Leonard et al. [2007]).

GPS velocities indicate that the Yakutat Indentor is moving to the northwest at 43.9 $\pm$ 2.9 mm/yr with respect to stable North America, and a considerable portion of this strain ($\sim$31 mm/yr) is accommodated between the coast and the Denali fault, mostly in the St. Elias and Chugach fault system (Leonard et al. [2007]). Some of the strain, however, may be transferred further northeast through the Cordillera causing renewed uplift in the MM (Mazzotti and Hyndman [2002]). Geodetic measurements show that stations in Yukon Territory exhibit 5-10 mm/yr northeastward motion with respect to stable North America (Leonard et al. [2007]; Marechal et al. [2015]) consistent with a “strain knot" induced by the Yakutat Indentor which rotates the strain field to the NE (Marechal et al. [2015]).

In contrast to the central Cordillera, the MM are seismically active (Mazzotti and Hyndman [2002]; Leonard et al. [2007]) (Figure 4.7). Seismically inferred convergence rates of $\sim$1-5 mm/yr oriented north to northeast within the MM (Leonard [2006]; Leonard et al. [2008]) agree well with the predicted direction of strain transfer from the Yakutat collision zone. Seismicity is also observed in the Richardson Mountains north of the MM along strike-slip faults oriented north-south (Mazzotti and Hyndman [2002]). This evidence of active seismicity, and the transfer of strain $\sim$750 km inboard of the active plate boundary with a lack of significant deformation in the central Cordillera make the MM an excellent location to study the processes that produce an intra-plate orogen.

There are two major hypotheses for the ongoing deformation in the MM, while a third explains the deformation episode that occurred $\sim$30 Ma, but may have some relevance for ongoing orogenesis. The first hypothesis invokes a process called “orogenic float" (Oldow et al. [1990]) where strain induced by the Yakutat Indentor is transferred to the NE along a weak detachment between the upper and lower crust (Mazzotti and Hyndman [2002]). The hypothesis, therefore, proposes the existence of a décollement in the lower crust that rises under the MM fold and thrust belt link-

ing the faults within the orogen to the plate boundary, thus enabling the transfer of strain. Gravity modelling provides some evidence for the existence of a décollement that shallows to the NE (Hayward [2018]). The second hypothesis proposes that asthenospheric flow from under Alaska is deflected eastward by the eastern edge of the subducting Pacific slab towards the MM causing convergent basal tractions under the MM (Finzel et al. [2015]). According to the third hypothesis, the Oligocene-early Miocene deformation in the eastern NCC can be explained by southwestward horizontal forces emerging from the opening of the North Atlantic Ocean which pushed the Canadian craton under the weak Cordilleran crust causing crustal deformation and uplift in the MM (Enkelmann et al. [2019]).

Understanding the processes causing orogenesis has, until recently, been limited since few geophysical data exist within the MM. Global tomography, heatflow, and elastic thickness modelling all show a distinct transition between a strong and cold craton, and a weak, hot, and thin lithosphere, roughly bounded by the deformation front (Schaeffer and Lebedev [2014]; Lewis et al. [2003]; Hyndman et al. [2005]; Hyndman [2010]). Several tomography studies show a rapid transition from high velocity mantle to the NE of the deformation front to low velocities to the SW (Schaeffer and Lebedev [2014]; McLellan et al. [2018]; Bao et al. [2014]). Further evidence of a sharp discontinuity between the Cordillera and craton comes from heat flow measurements which yield high values west of the deformation front (105 ± 22 mW/m^2), and low values to the east ($\sim$53 mW/m^2) (Lewis et al. [2003]; Audet et al. [2019]). Heat flow also increases noticeably north of 59°N latitude (Lewis et al. [2003]) which coincides with the location of the LTZ. Estimated Moho temperatures based on these heat flow measurements are $800 - 900^{\circ}$ under the Cordillera and $400 - 500^{\circ}$ C under the craton (Lewis et al. [2003]). Because the crustal thickness is found to be fairly consistent ($\sim$35 km) in the Cordillera, the high elevations here are attributed to density reduction due to higher temperatures (Hyndman [2010]). These temperature variations also govern the effective elastic thickness (20 km for the Cordillera and $\sim$100 km for the craton) (Fluck et al. [2003]; Audet et al. [2007]).

There are some notable hints that more complex structure than just a hot/cold dichotomy exists in the region. A high velocity anomaly just west of the Tintina fault that coincides with the accreted Intermontane terrane is imaged by a more recent surface wave study (McLellan et al. [2018]). Deep structures such as a 250 km wide high S-wave velocity feature at $\sim$150-200 km depth beneath the southern Cordillera may indicate lithospheric delamination due to mantle upwelling (Bao et al. [2014]). Notably, tectonic models show the development of a slab window under the NCC (Figure 4.9) starting about 20 Ma (Thorkelson and Taylor [1989]; Thorkelson et al. [2011]), which coincides with the onset of active volcanism in the western Cordillera (Edwards and Russell [2000]) (Figure 4.7).

In this paper, we present the first body wave tomographic results that include data from the Mackenzie Mountains Earthscope Project (MMEP). This joint geodesy and seismology project involved a line of 40 seismometers and 4 continuous GPS stations that were deployed along a NE directed array from near the coast to the Slave Craton (Baker et al. [2019]) (Figure 4.8). The stations are the first to transect the Mackenzie Mountains, and collected data from July 2016 through August 2018 with three stations operating till August 2019.

2.2 Data and Method

We downloaded data from 104 seismic stations in the NCC from arrays including the Mackenzie Mountains Earthscope Project (DOI: 10.7914/SN/7C_2015), the Canadian National Seismograph Network, the Yukon Northwest Seismic Network (DOI: https://doi.org/10.7914/SN/NY), the Earthscope Transportable Array, the Canadian Northwest Experiment, and the Yukon Observatory (Owens et al. [2004]; Baker et al. [2019]). The phases requested were P, PP, S, SS, and SKS. Events with magnitude >5.2, and signal to noise ratio >2.5 were used. Angular distance range was 35°-100° for P, PP, S and SS phases, and 80°-125° for SKS. The mean, trend, and instrument response were removed and all data were down-sampled to 20 Hz to reduce processing time. The traces were cut at -25s and +25s about the first arrival predicted by PREM (Dziewonski and Anderson [1981]). Events that were detected at 5 or more stations were bandpassed with corner

frequencies 0.1 Hz - 2 Hz (P-waves), 0.05 Hz - 0.4 Hz (S waves), and cut at -15s to +15s around the first arrival.

To prevent interference, traces were excluded where a second phase arrival was predicted within six seconds of the first arriving phase. Cross-correlation was used to cull events and traces with weak or inconsistent signals. This process resulted in identifying 180 P-phase and 486 S-phase events (Figure 4.10). For these events, relative travel time residuals were calculated using the method of multi-channel cross-correlation (VanDecar and Crosson [1990]). In total 4140 V_p and 8250 V_s residuals were measured.

We used the "Fast Marching Tomography" code (Rawlinson and Sambridge [2005]) to invert these residuals and their uncertainties to produce the P-wave and S-wave velocity models below the NCC. The objective function that the inversion tries to minimize is,

$$S(m) = \frac{1}{2}[\psi(m) + \epsilon\phi(m) + \eta\Omega(m)], \tag{2.1}$$

where ϵ is the *damping factor*, and η is the *smoothing factor*. The vector m is the model vector of unknowns that are adjusted during the inversion.

The first term on the right hand side (RHS), ψ(m), is

$$\psi(m) = (g(m) - d_{obs})^T \mathbf{C}_d^{-1}(g(m) - d_{obs}), \tag{2.2}$$

where C_d is a data covariance matrix, and $g(m)$ is a vector of traveltime predictions associated with the model defined by m.

The second term on the RHS, ϕ(m), is

$$\phi(m) = (m - m_0)^T \mathbf{C}_m^{-1}(m - m_0), \tag{2.3}$$

where C_m is an *a priori* model covariance matrix. The effect of $\phi(m)$ is to encourage solution models *m* that are near a reference model m_0 (in this case a starting model).

The last term on the RHS in equation (1), Ω(m), is

$$\Omega(m) = m^T \mathrm{D}^T \mathrm{D} m, \tag{2.4}$$

where D*m* is a finite difference estimate of a specified spatial derivative. Here, D is the second derivative operator. So, Ω(m) reduces in size as the model becomes smooth.

We carried out inversions for V_p and V_s with AK135 (Kennett et al. [1985]) as the starting model. To consider the trade-off between model norm and variance reduction we ran each inversion with different values of damping. All other parameters such as smoothing, number of velocity nodes, model depth, and number of iterations were held constant. The damping values at the corner of the trade-off curves (Figure 4.13 and Figure 4.19b) were used to produce the final results.

2.3 Results

2.3.1 P wave results

Travel time residuals vary from -2.05 s to 1.85 s, and have a standard deviation of 0.43 s. Residuals for events arriving from the northwestern quadrant show an almost periodic trend along the MM array (Figure 4.11a) suggesting that significant velocity heterogeneity exists west of the deformation front. Starting from 134.55°W, 60.24°N, the location of station MM04, the residuals remain negative until ∼234 km which is roughly the location of the Tintina fault. Northeast from the Tintina the residuals become positive until the Cordilleran deformation front is reached at ∼600 km. The TA stations to the northwest, however, show anomalously high velocities (Figure 4.11b).

2.3.1.1 Perturbations with respect to AK135

Figure 4.14 and Figure 4.15 show the model obtained with the optimal damping. Total variance reduction is 72.5%. The notable features are: 1) the high velocity feature under Tintina fault at 134°W, 61°N labeled “F1". 2) the horizontal high velocity feature at 600 km depth labeled “F2". 3) the high velocity Canadian craton labeled “F3", and 4) the high velocity feature in north-central YT.

2.3.2 S wave results

A total of 8250 residuals were used in this study. Residuals varied from -3.83 s to 3.83 s, and had a standard deviation of 1.03 s.

2.3.2.1 Perturbations with respect to AK135

Perturbations in map view (Figure 4.24) show the same patterns as the P wave results, however the amplitudes are higher. The cross sections show more vertical smearing mostly due to a large number of SKS arrivals and hence the high velocity anomaly F2 is not labeled in Figure 4.25. This is the model obtained by using the damping value at the corner of the trade-off curve yielding a variance reduction of 67.35%.

2.3.3 Resolution Tests

2.3.3.1 P waves

To assess the resolution of our models we carried out checkerboard tests. Alternating $\pm$ 0.2 km/s anomalies were superimposed on AK135 (Kennett et al. [1985]) and travel time residuals were calculated through this model. These residuals were inverted, using the same damping and smoothing values as those used in the actual inversion, to recover the checkerboard (Figure 4.16). A slice at 600 km is taken to visualize the recovery of the high velocity checkerboard anomaly at that depth because it corresponds to the location of the high velocity feature in Figure 4.15. Note the absence of structure resolved in west, north and northeast portions of the model due to the absence of stations.

In map view (Figure 4.16), the anomalies are recovered well spatially except at 600 km depth. The 30 km, 50 km, and 120 km depth slices show similar average recovered amplitudes ($\sim$40%) whereas at 75 km depth, the recovery is slightly better ($\sim$50%).

Recovered checkerboard along the MM array is shown in Figure 4.17b. The recovery is good in the upper 200 km due to the abundance of stations along this line, and amplitude recovery is about 50% of the input amplitudes. The high velocity feature at depth, however, is not recovered.

An east-west cross section along 64°N latitude showing some smearing along the ray paths and generally good recovery within the longitude range of 220°E to 240°E (where station density is highest) is shown in Figure 4.18. Notice the change in color scale between the input and output checkerboards.

Although the checkerboard recovery variance reduction is 55%, the lateral resolution of the model is good and allows us to interpret the anomalies in the lithosphere with confidence, especially under the MMEP stations. However, the east-west cross section shows more limited depth resolution because of a scarcity of stations parallel to the cross section line.

2.3.3.2 S waves

The S wave ray paths recover the high velocity at 600 km depth with much better lateral resolution which is most likely because of a higher number of ray paths compared to P waves. The high velocity structure in the upper 200 km is also recovered very well with an average amplitude of 0.2 km/s. Figure 4.23b shows the recovered checkerboard along the same EW cross section as before. Note that the better ray path coverage is able to recover anomalies with a higher amplitude than in the case of the P wave checkerboard. The total variance reduction is 87%

2.4 Discussion

The west to east transition from low to high velocities doesn't coincide with the Cordilleran Deformation Front but appears to be ∼75 km to the southwest (Figure 4.14). A cross section along the MM stations (Figure 4.15) shows the presence of high velocities under the NE part of the MM. This may be a strong cratonic backstop that halts the NE-ward motion of the upper crust, causing uplift (Mazzotti and Hyndman [2002]). It's notable that the lithosphere between the deformation front and the Tintina fault is not uniformly of low velocity, but rather the low velocities seem to be located primarily along the central part of the MM. This suggests the region of weak lithosphere is laterally constrained, most notably by the high velocities to the NW of the MM which may be an extension of the Mackenzie craton proposed by McLellan et al. [2018]. Ongoing deformation from

the Yakutat indentor may be focused by this region of low velocities, causing the arcuate nature of the MM.

The low velocities in the southwestern part of the model nearly always underlie areas of recent (<20 Ma) volcanism. A notable exception, however, are the volcanoes under western Yukon and eastern Alaska (Figure 4.14a). Also, the regions of low velocity in the 50 km and 75 km V_p images tend to be of consistent magnitude. If the asthenosphere under the regions of active volcanism is near the solidus, then it is possible that much of the upper mantle under the MM, which has similar velocities, is at a similar temperature.

The high velocity feature “F1" coincides with the location of the Intermontane terrane (Figure 4.26). The sharp contrast in velocity across the Tintina fault suggests that it may be a compositionally distinct unit of lithosphere that has been translated ∼400 km northwestward by Eocene slip on the Tintina. Presence of this anomaly is corroborated by the ambient noise tomography results in the region which show a high velocity feature in the same location at mid-crustal depths (McLellan et al. [2018]).

We interpret the second high velocity anomaly “F2" as delaminated lithosphere. In the southern Cordillera, convective mantle upwelling along the edge of the craton is thought to have caused lithospheric delamination ∼55 Ma (Bao et al. [2014]). Within the region of this study, the opening of the slab window in the Oligocene-early Miocene (Thorkelson and Taylor [1989]; Thorkelson et al. [2011]) could have led to asthenospheric upwelling and subsequent removal of part of the lithosphere. This would explain the thin and hot lithosphere inferred by many studies (Lewis et al. [2003]; Hyndman et al. [2005]).

Additionally, the opening of this window explains much about the recent volcanism: the timing of the window coincides with the spread of volcanism (Edwards and Russell [2000]; Thorkelson et al. [2011]); the source is identified as asthenospheric (Edwards and Russell [2000]), suggesting a shallow lithosphere-asthenosphere boundary, and geochemical analysis suggests anhydrous melting that coincides spacially with the slab window (Thorkelson et al. [2011]) (Figure 4.9).

According to Enkelmann et al. [2019], the current phase of uplift in the MM is the fourth since the Cretaceous. Assessing the cause of the ongoing uplift is challenging. It's notable that Lithoprobe studies found little or no offset of the Tintina Fault to the NW (Cook et al. [2004]), suggesting that if orogenic float is causing the current deformation there has been little lateral translation of the upper crust. While data are limited, there is no evidence of recent cooling from geochronology (Enkelmann et al. [2019]), which may imply that the current uplift has not produced significant unroofing of deeper rocks. A possibility is that the arrival of the slab window around 20 Ma led to delamination of the lithosphere in a narrow region under the MM. This region of weak lithosphere focused strain from the Yakutat Indentor, causing uplift to initiate only recently, in which case total shortening from modern uplift would be quite small. If the Tintina fault is truly not offset to the NE, even after $\sim$10-30 My of Yakutat subduction, this would imply the lithosphere to the east of the Tintina was too strong for NE-directed crustal strain transfer until quite recently. Alternatively it is possible that the upper crust here is indeed offset to the NE, but this has not been imaged. In either case, we would suggest that a 3-D version of the orogenic float model should be explored, since lateral lithospheric velocity variations, and hence lateral strength variations, are significant.

It's also notable that a weak lower crust, as proposed by Mazzotti and Hyndman [2002], would decouple the effects of asthenospheric tractions from the upper crust (Finzel et al. [2015]). However, the high velocities under the NE portion of the MM may imply a lower crust that can transfer stress from the lithospheric mantle to the upper crust, allowing for deformation as proposed by Finzel et al. [2015]. Any mechanism invoked for MM uplift, however, will have to consider the complications of a heterogeneous lithosphere, as well as the potential effects of asthenospheric convection as hot material upwells in response to the sinking cold blob identified in our images as "F2".

2.5 Conclusions

Our teleseismic body wave tomography results show distinct and large velocity anomalies below the NCC. A NE-directed tongue of low uppermost mantle velocities extends under the central part of the MM but doesn't correspond to their lateral extent. It is limited by a sharp high velocity feature at the NW corner of the MM, and a broad but more subtle zone of higher velocities under the southern MM. Together, these features could focus Yakutat-driven orogenic float along the low velocity zone. A cratonic "backstop" that could trigger uplift from NE-directed upper crustal motion (Mazzotti and Hyndman [2002]) is found under the NE-most part of the MM. This may also be a location where basal lithospheric tractions can be coupled and lead to surface deformation (Finzel et al. [2015]). Our velocity model does not specifically identify the cause of the ongoing orogenesis, but it does show that the NCC cannot be modeled as a dichotomy between strong and cold cratonic lithosphere NE of the deformation front and weak and hot lithosphere to the SW. The $\sim$5% V_p variations at 120 km depth suggest large temperature variations, of at least 200 °C (e.g. Karato [1993]).

Additionally, a lithospheric high velocity feature is imaged along the Tintina fault which may represent a fragment of the lower crust or mantle lithosphere translated by Eocene dextral slip along the fault. This suggests that the process of terrane accretion and dextral transpression (Nelson et al. [2013]) may have created long-lasting lithospheric strength and compositional heterogeneities.

The high velocity feature at $\sim$600 km depth may indicate a chunk of the Yukon mantle lithosphere that delaminated in response to a slab window that migrated under the region about 20 Ma. Alternatively this may be a fragment of a subducted slab. In either case, upwelling in response to the slab window may have created the tongue of low velocities, which may be focusing strain induced by the Yakutat Indentor. In this scenario, it may be that the slab window and consequent loss of part of the MM lithosphere was necessary for orogenic float re-initiating MM uplift. Although more data are needed, the lack of a thermal signature associated with the current phase of uplift (Enkelmann et al. [2019]) may imply that conditions causing the current uplift have only persisted for a few M.y.

Chapter 3

3.1 Future Work

There are many more graduate level projects that can further our understanding of the northern Canadian Cordillera. Because seismic velocities are a function of temperature, the 3D body wave velocity model acquired in this study can be used to calculate lithospheric temperature variations using the temperature derivatives of seismic velocities from Karato [1993]. A concrete constraint on temperatures could help in determining the extent of melt under the volcanoes in the NCC, and may also substantiate the orogenic float hypothesis depending on the calculated crustal and upper mantle strength profile.

Attenuation is another important phenomenon which needs to be studied and refers to the conversion of seismic wave energy into heat resulting in its decay. Body wave attenuation is characterized using,

$$t^* = t/Q \tag{3.1}$$

where *t* is the travel time and Q is the quality factor. t^* is directly proportional to the degree of attenuation and is calculated by integrating along the ray path,

$$t^* = \int dt/Q \tag{3.2}$$

Temporary seismographs can be deployed in the region with spacing of the order of a few kilometres to acquire a more detailed velocity model of the crust while receiver function studies can constrain the Moho depths which will be crucial to map the crustal root of the MM. Once the Moho is mapped in detail, refracted seismic head waves from the base of the Moho can also be used to calculate velocities and hence temperature at the base of the Moho. Shear wave splitting studies can further our understanding of the crustal and upper mantle anisotropy which is very important given the complex tectonic history of the region. For example, strike-slip faults and

absolute plate motion impart shear in the crust/upper mantle and asthenosphere respectively which can be imaged using this method.

Earthquake detection can bring to light previously unknown fault planes and will be useful to monitor the seismic activity in this region. Data from these earthquakes can be used for local tomography which will significantly improve the depth resolution in the present models as more horizontal ray paths will be available in addition to the vertical ray paths from teleseismic arrivals. More geodetic instruments can also be deployed within the MM to analyze small scale differences in rates and directions of convergence. All these different projects will significantly improve our understanding of this entire region.

3.2 Data Processing Sequence

This section includes the overall workflow and guidelines on using some of the bash and Matlab scripts used in the process. All the necessary scripts for steps 1 to 9 below are in: "/data/seismo/Adi/scripts/MM_tomo_scripts" and well-commented. The "Master_MM_tomo.bash" script in this directory can do steps 2 to 9 at once. This script is also well commented and will prompt the user about the parameters that need to be adjusted prior to running it. The folder "fmtomo_NEW" in this directory contains the compiled FMTOMO code used for the inversion. The overall processing sequence is as follows:

1. Download raw data. The Standing Order for Data (SOD) recipes have file names of the format- "first_*phase*_arrival_MM.xml" where the word "*phase*" is replaced by the specific phase name. When data is downloaded, individual folders for each event are created and the name of each folder will begin with the year the particular event took place.

2. Remove duplicate files using the script "Remove_duplicate_files.bash". If for a station, both "HHZ" and "BHZ" files are present, the script will delete the "HHZ" file (or move it to another specified directory if the user edits the script accordingly).

3. Run “Bandpass_raw_traces.bash". The script will bandpass the traces based on the corner frequencies specified by the user.

4. Run “non_overlapping_events.bash". This script identifies traces where the phase of interest is separated from other phase arrivals by at least 6 seconds. This time separation can be adjusted.

5. Run “find_good_events.m" for multi-channel cross-correlation. The parameters and directories that can be changed are at the beginning of the script. However, other than the directories, the only parameter that was adjusted for this project was “err_max" which is the maximum allowed error (0.4 for P waves and 0.8 for S waves).

6. Run “make_receiver_table.bash". It loops through each event, reads each sac file, and creates a table of elevation, latitude, longitude, and station name.

7. Run “get_resids.m". This script calculates the travel time residuals for each trace, and creates pdf plots for each event showing the traces aligned on the actual first arrival. Adjustable parameters and directories are at the beginning of the script.

8. Run “make_pick_files.m" This script creates the pick files which are the input to FMTOMO. In addition to the directories, user will need to update the phase name on lines 9, 10, and 18.

9. Run “flip_residual_signs.bash" which changes the signs of the residuals calculated by the matlab script in step 7 above. If the original residuals are used in the inversion, the craton shows negative velocity perturbations while the Cordillera shows positive velocity perturbations which is, of course, not accurate.

10. Do the inversion using FMTOMO and plot the results using the provided GMT scripts. The directory “/data/seismo/Adi/scripts/MM_tomo_scripts/fmtomo" contains the necessary files to run the code while “.../fmtomo/gmtplot" contains the GMT scripts to plot the results.

The following steps are necessary in order to run FMTOMO:

1. The “grid3dg.in" file creates the input 3D model (lat-long bounds, depth in km, number of velocity and interface nodes are some examples of free parameters found in this file). The number of interfaces must be *n*+1 where *n* is the number of layers in the model. The topmost interface must be a few km above the earth’s surface to account for topography, and the bottom interface must be slightly above the lowermost depth bound of the model. Also, the number of interface nodes in lat-long must be equal. For this project, the topmost interface was 5 km above the earth’s surface, the bottom interface was 0.1 km above the lowermost depth bound of the model, and 22 nodes spanned each interface in latitude and longitude.

   As far as velocity nodes are concerned, user can choose the number of nodes in latitude, longitude and depth. It is also possible to choose velocity values from an external model (including the “AK135") or use a constant gradient. For this project, number of nodes in depth, latitude and longitude was 11, 22, 52 in the crustal layer and 12, 22, 57 in the mantle. These numbers were chosen to make each 3-D cell in the model region roughly cubic which also helped fit the data a little better. Note that the code automatically adds cushion nodes on either sides and hence the actual number of nodes became 13, 24, 54 and 14, 24, 59. Lastly, the switch to turn checkerboard, and spikes on/off for velocity layers and interfaces is also present in this file which will be useful to carry out synthetic tests. After you update this file based on your needs, execute the “grid3dg" program. It produces three of the required files for the inversion- “propgrid.in", “vgridsref.in", and “interfacesref.in". The “cushion factor" parameter in “grid3dg.in" is also important. If you get an error regarding the propagation grid, the cushion factor may need to be changed slightly (note that it has to be $<<1$). For this project, it was set to 0.04. Lastly, note that the propagation grid also should be roughly cubic, and the number of nodes in this grid primarily controls the speed of computation. For this project, in the beginning, an 80x40x40 grid was chosen which was changed later to 30x30x30 resulting in a staggering 8x decrease in computation time.

2. Edit “residuals.in". The only change that needs to be made is changing the filename “rtimeso.dat" to “rtimes.dat". When the forward problem is solved, FMTOMO stores the predicted travel

times through your input model (defined by “interfacesref.in" and “vgridsref.in") in this auto-generated “rtimes.dat" file. However, if the model region has significant travel time contributions from the topography, the user may make his/her own predicted travel times to account for these changes and store them in “rtimeso.dat". For this project, auto-generated “rtimes.dat" file was used.

3. Edit “obsdata.in". User should make a sub-directory in the working directory called “picks" to store the pick files. The path to this subdirectory is mentioned in “obsdata.in". The next parameter “number of input files" was set to 1 for this project as only teleseismic events were used. If local events are also present, the user will need to make two input files, and the parameter should be set to 2. Explanation on how to construct the input files and pick files for local and teleseismic events is given on pages 41-47 of the FMTOMO manual. The parameter “number of paths from these sources" was set to 1 as all teleseismic events were at least 35° away from the receivers, and hence all the arrivals were vertically incident. However, in case of local tomography where shallow reflections and refractions occur, the number of paths will increase depending on the phase arrivals. The next parameter, “number of path segments" was set to 2, as the vertically incident rays went from interface 3 to interface 2, and then from interface 2 to interface 1. See the FMTOMO manual pages 38-39 for an explanation on setting the path signatures and path segments.

   After you update this file based on your needs, execute the “obsdata" program. Note that if you change the latitude-longitude-depth bounds of your input model or if you’re going from P wave phases to S wave phases, “obsdata" needs to be run. One important thing to consider is that the “receivers.in" file that “obsdata" generates contains lat-long coordinates of the receivers. Its important that the longitudinal coordinates of these stations are defined as east of the meridian (e.g. 220° etc). The user will need to change these numbers after this file is made by “obsdata". The number on the first line of “receivers.in" is the total number of travel time residuals.

4. Edit “invert3d.in" as required. It contains all the important parameters required for the inversion such as the damping factor, smoothing factor etc. It also lets you choose to invert for interfaces and the source locations. For this project, the interface inversion and source inversion switches were off.

5. Edit “tomo3d.in". The only useful parameter it contains is the number of iterations. For this project, 3 iterations were used for both P and S waves.

6. If you want to visualize the ray paths, that switch has to be turned on in the ‘mode_set.in’ file which is another required file and has to be present in the working directory.

Once you have all the required files in the working directory, execute “tomo3d". The “residuals.dat" file that tomo3d generates will record the variance at every iteration which will be useful to plot the trade-off curve. The recovered velocity and interface depth values are written in “vgrids.in" and “interfaces.in" respectively. An explanation of how vgridsref.in (input velocity file) and vgrids.in are made is given on pages 20-21 of the FMTOMO instruction manual. In a nutshell, the innermost loop is over longitude and outermost loop is over depth. So the first velocity value in these files corresponds to the SW point at the lowermost depth in your model.
[Note: When “tomo3d" is run, it first intrinsically runs the “fm3d" program which solves the forward problem and redirects the verbose output to “fm3dlog.out". The user should monitor this logfile and terminate the program in case any error statements are observed as this will most likely cause the inversion to break down. For example, if the word “ilong" appears in this file, that means there is an issue with the propagation grid and the “cushion factor" in “grid3dg.in" should be adjusted. Remember to run grid3dg, obsdata (and change the receiver longitudes to east of the Meridian), and then tomo3d in that order after any changes to your input model].

After the inversion is completed, the user has the choice to plot absolute velocities, linear perturbations (in km/s) or perturbations as percentage. If percent perturbations are to be plotted, the script “Make_output_vel_file.bash" needs to be executed first. The script is commented and is self-explanatory.

The GMT scripts are provided with FMTOMO to plot depth slices and cross sections through the model. The only program that the user needs to run prior to running these GMT scripts is “gmtslice", and the input file required is “gmtslice.in". There are a number of free parameters in this file such as lat-long coordinates of the starting and ending points of the cross section line(s) (these coordinates are mentioned in the “plotd" script which plots the depth slice), depth at which you want to take a horizontal slice, choosing whether to plot absolute velocities or perturbations, and whether to plot P or S wave velocities. If you wish to plot % perturbations, put the name “percent_perturb.in" in the first line of “gmtslice.in". When “gmtslice" is run, it produces “.xyz" grids and other important input files that are read by the GMT scripts. These scripts, however, were made for an older version of GMT and the user may need to update the commands according to the GMT version at the time of usage.

Chapter 4

4.1 Figures

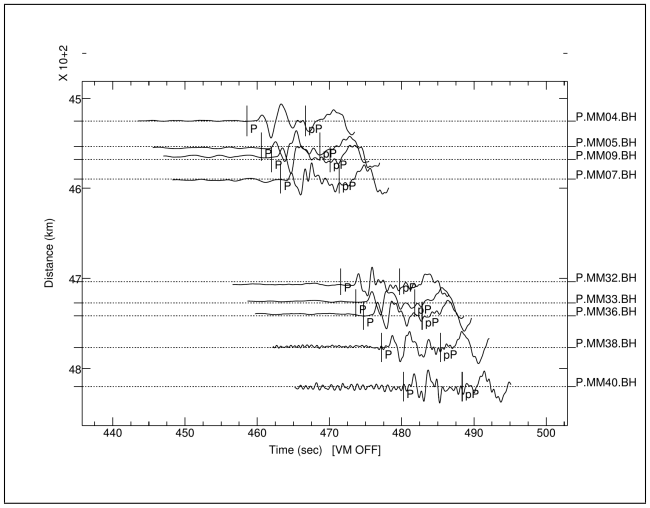

Figure 4.1: Record section showing direct P arrivals at stations in the NCC. x-axis is the time since the earthquake and y-axis is the distance to each station from the hypocenter.

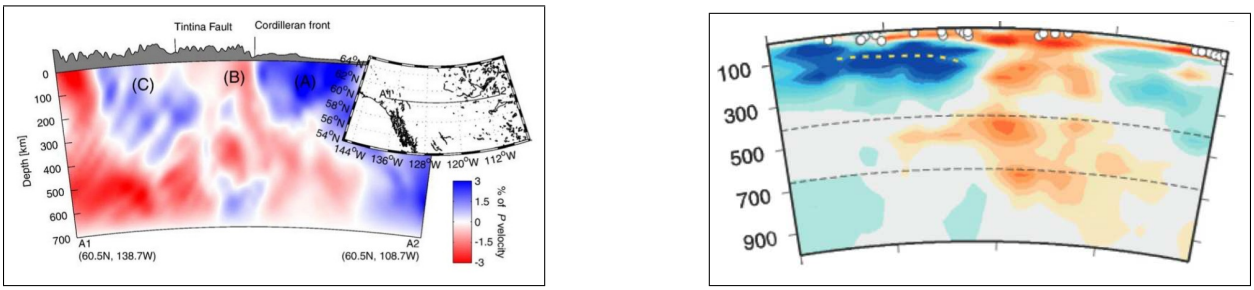

(a) **(b)**

Figure 4.2: (a) Body wave tomography results of (Mercier et al. [2009]) showing the Canadian craton labeled (A), a second high velocity anomaly to the left (C), and a low velocity anomaly of the southern Canadian Cordillera (B). (b) Subducting Indian slab seen on the left in blue owing to its low temperature which produces high seismic velocities (Wei et al. [2012]).

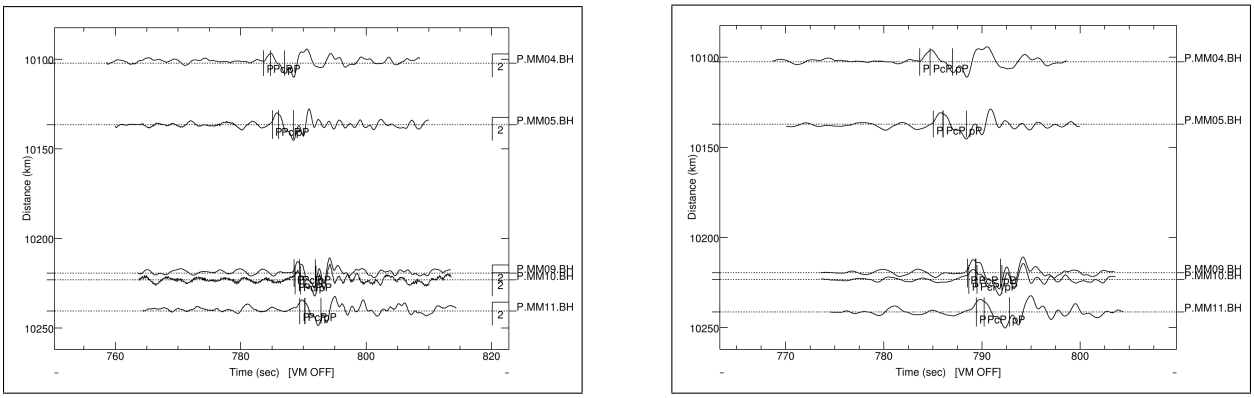

(a) **(b)**

Figure 4.3: (a) Raw data showing high frequency noise superimposed on the seismograms. x-axis shows the time in seconds since the earthquake, and the y-axis shows the distance from the hypocenter. Predicted arrivals of seismic phases P, pP, and PcP are shown on each trace. (b) Same seismograms bandpassed.

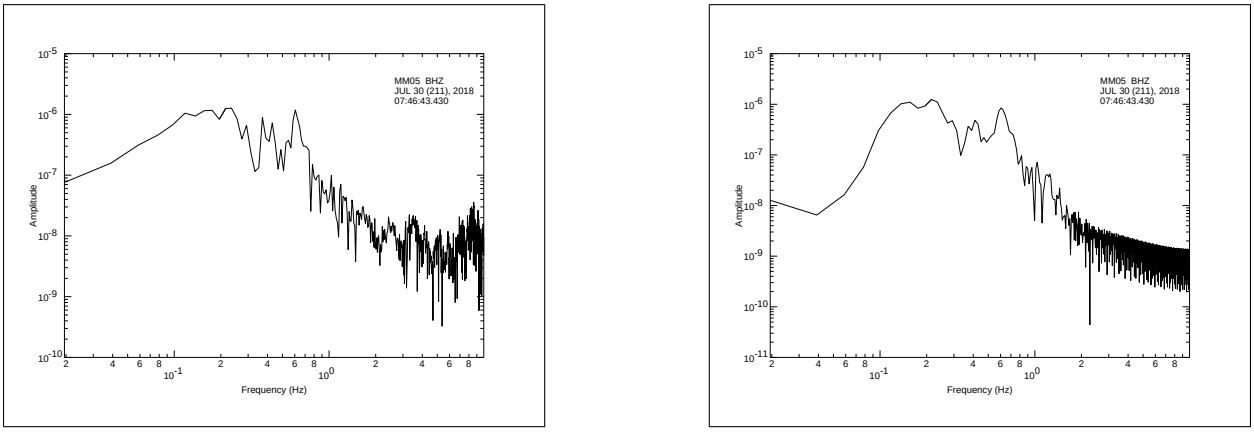

(a) **(b)**

Figure 4.4: (a) Spectrum of the raw trace at station MM05 from Figure 4.3a above. (b) Spectrum of the same trace after bandpassing.

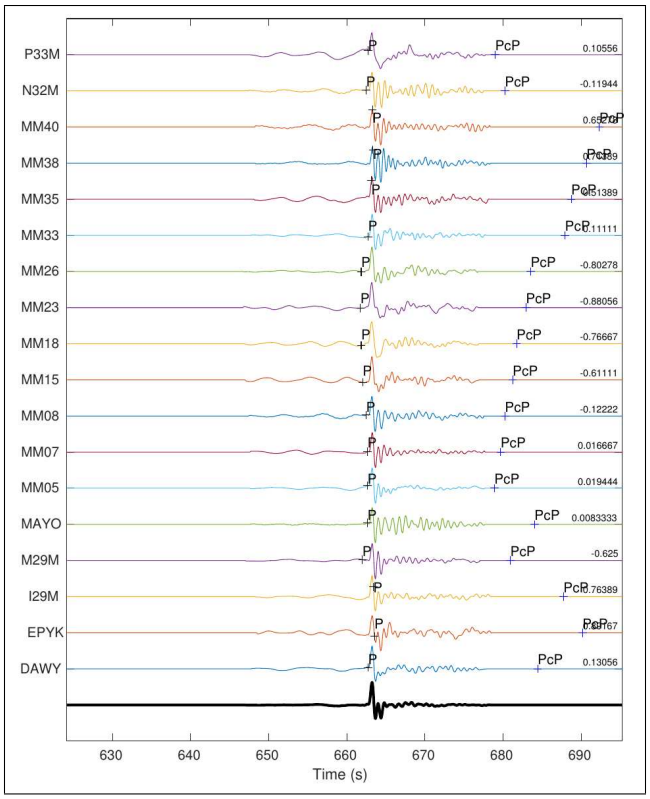

Figure 4.5: Plot of traces aligned on the observed direct P arrival. The numbers on the right at the top of each trace are the travel time residuals in seconds. Labels on the left are the station names.

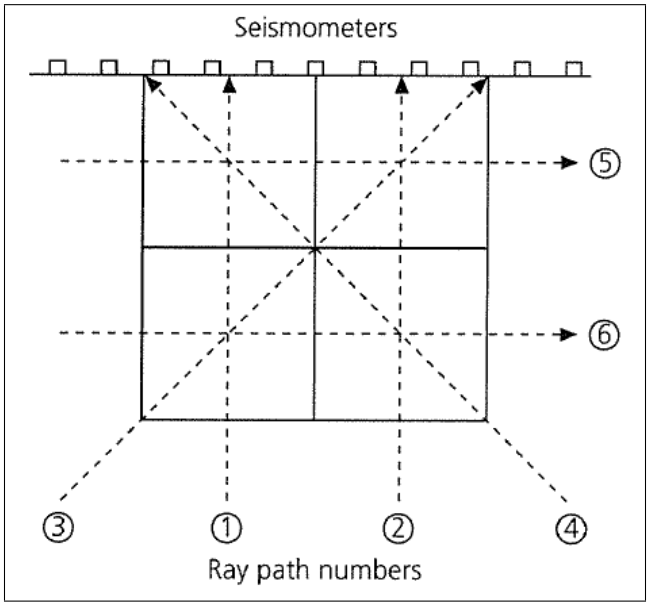

Figure 4.6: A vertical cross-section showing the seismometers at the surface and a 2x2 grid below. It is traversed by 6 rays shown as dashed lines (Stein and Wysession [2003]).

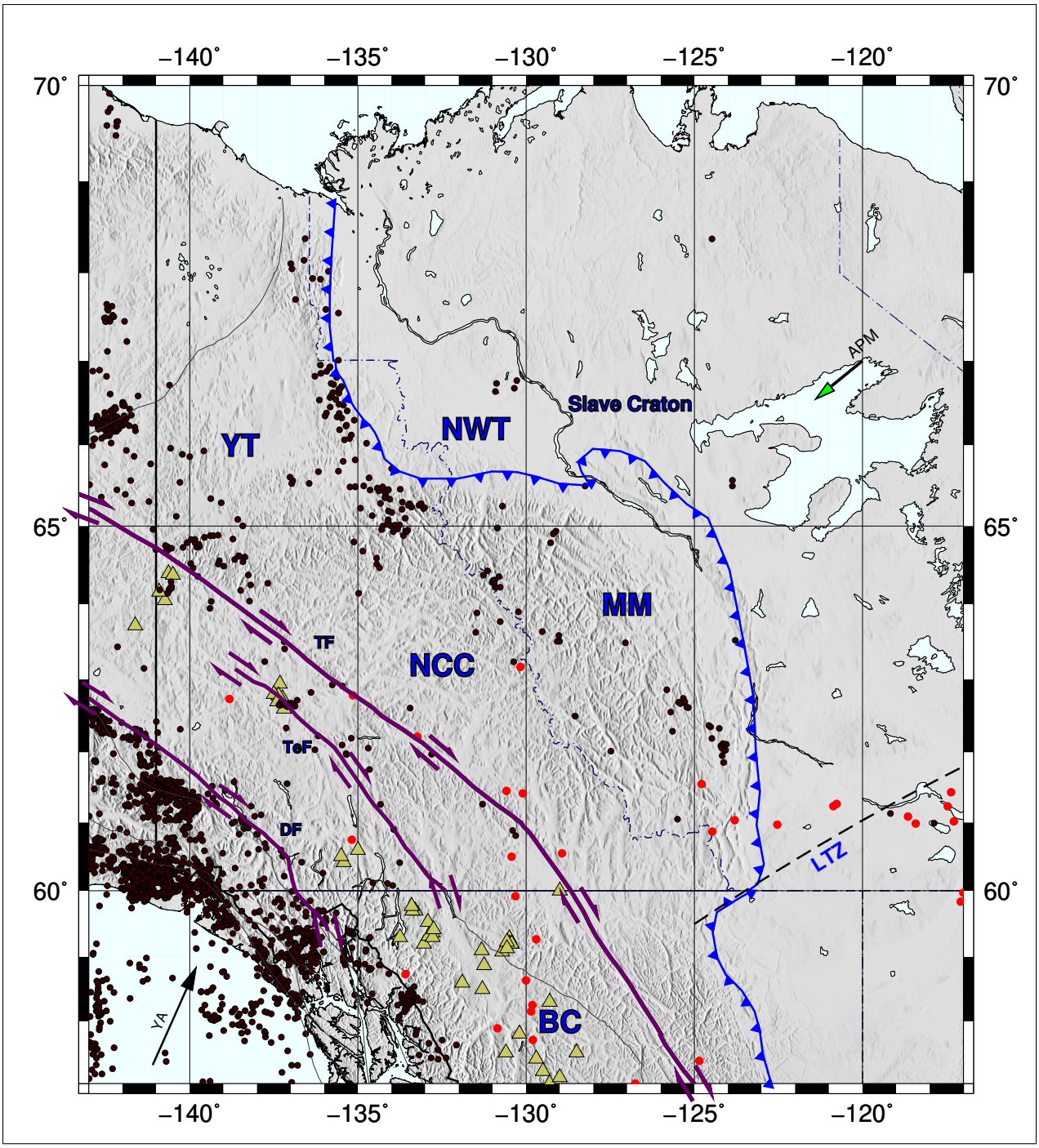

Figure 4.7: Tectonic setting of the NCC. The curved solid line is the Rocky Mountain Deformation Front and separates the NCC from the adjacent Canadian craton. Black dots are earthquakes from the year 2000 to 2018, red dots are the locations of heat flow measurements of (Lewis et al. [2003]), and yellow triangles are the volcanoes from the northern Cordilleran volcanic province. The three major strike slip faults Tintina (TF), Denali (DF), and Teslin (TeF) are shown as purple lines. The arrow in the SW corner shows the direction of strain transfer from the subduction zone, while the arrow in the NE denotes the absolute plate motion of North America. MM= Mackenzie Mountains, YT=Yukon Territory, NWT=Northwest Territories, LTZ=Liard Transfer Zone, BC=British Columbia, YA=Yakutat Indentor, APM=Absolute Plate Motion.

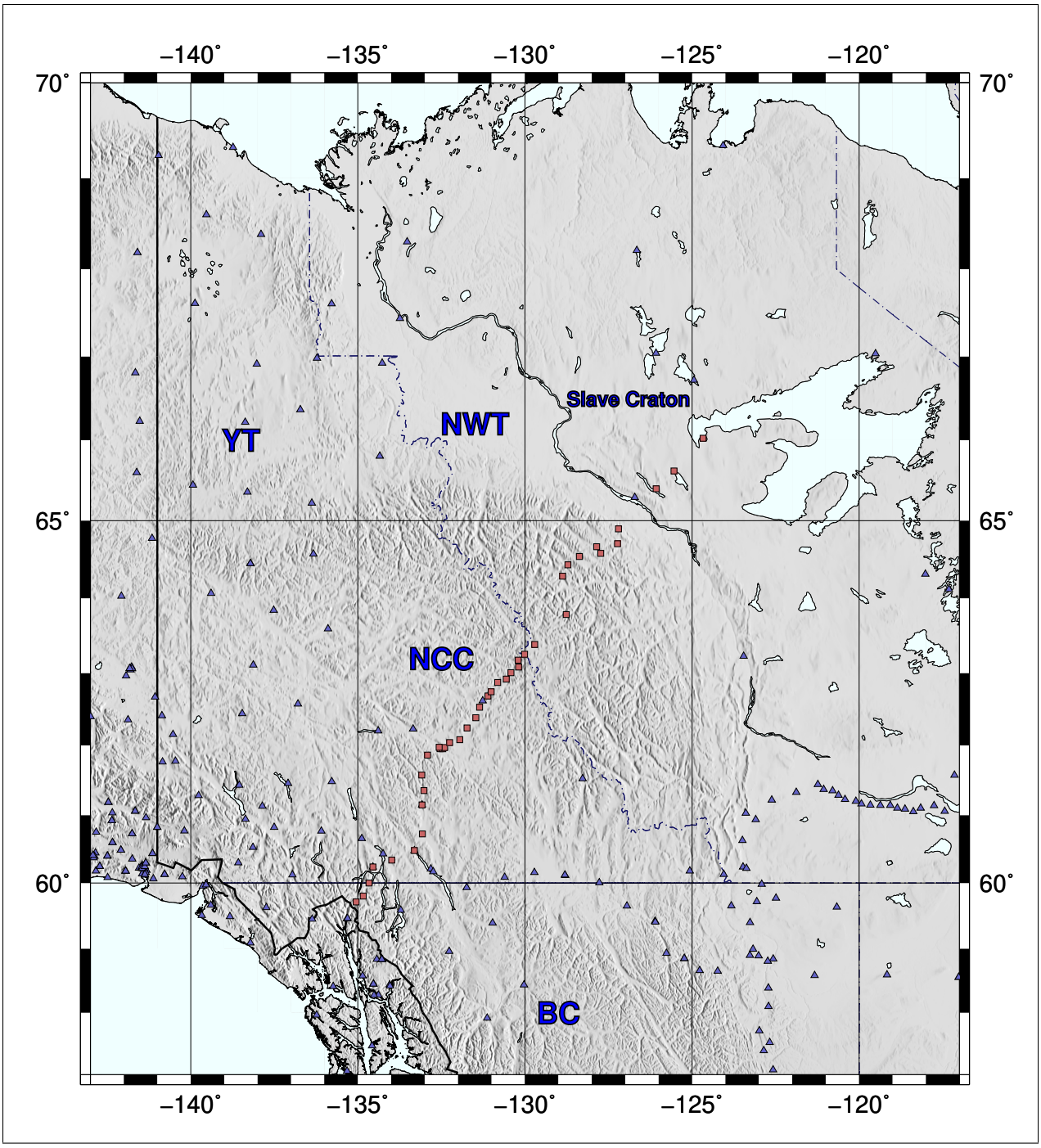

Figure 4.8: Map showing the locations of stations in the NCC. The MMEP stations are shown as squares. Triangles are stations on other networks.

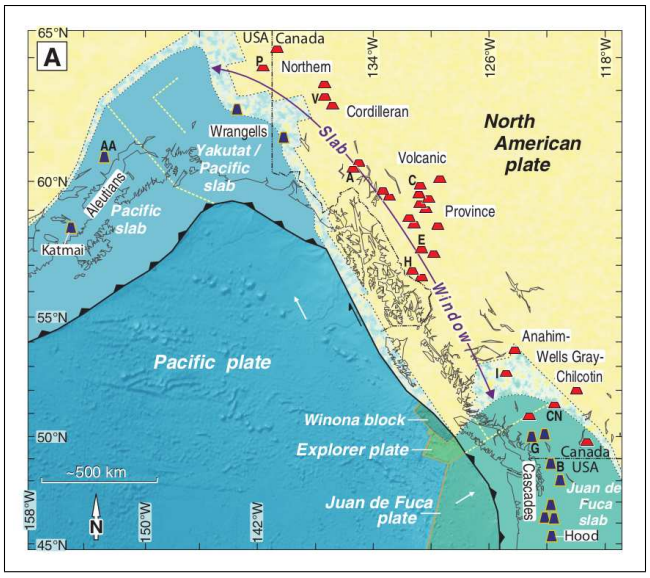

Figure 4.9: The proposed extent of the slab window underneath western North America. The red symbols are locations of the volcanoes. The white arrow in the center denotes the movement of the Pacific plate with resepct to stable North America (Thorkelson et al. [2011]).

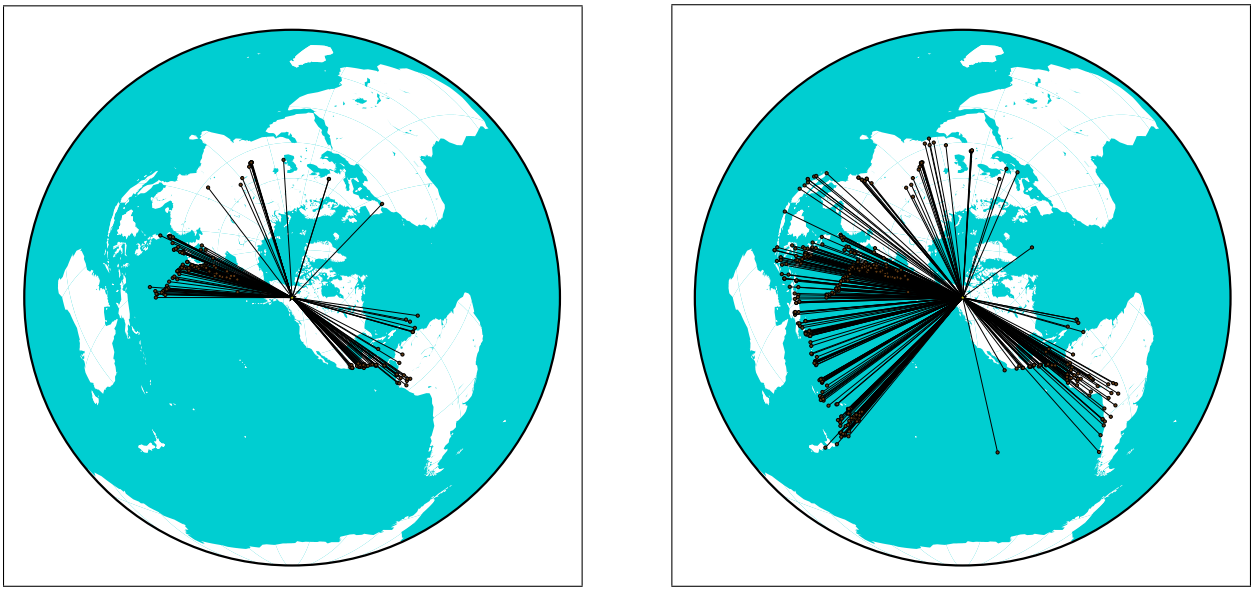

(a) **(b)**

Figure 4.10: Backazimuthal distribution of (a) 180 P phase events and (b) 486 S phase events.

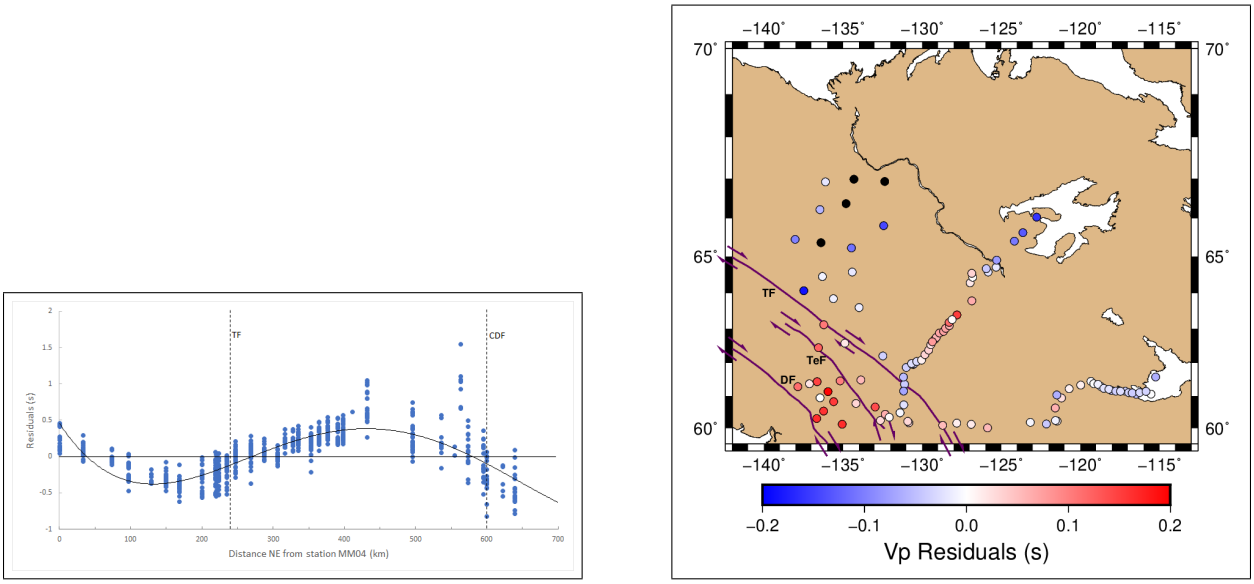

(a) **(b)**

Figure 4.11: (a) P wave residuals for events from the west as a function of distance along the MM transect. The curve is fit based on visual inspection of the trend. Vertical dotted lines indicate the locations of Tintina fault (TF) and the Cordilleran Deformation Front (CDF) (b) Mean P wave travel time residual at each station in the NCC. TF=Tintina fault, TeF=Teslin fault, DF=Denali fault.

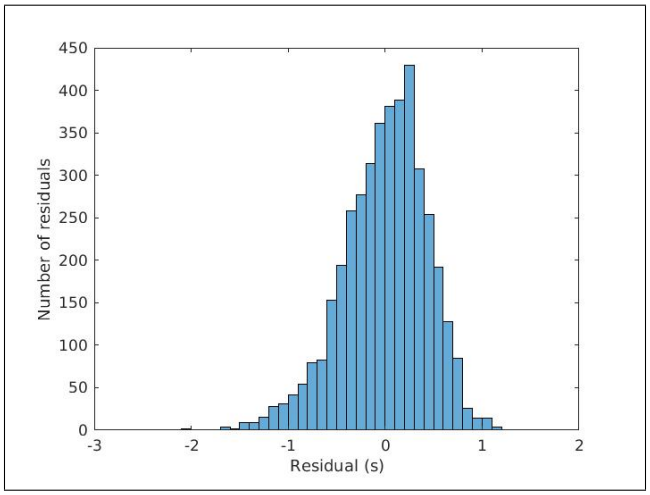

Figure 4.12: Histogram of all 4140 relative P wave residuals used in this study.

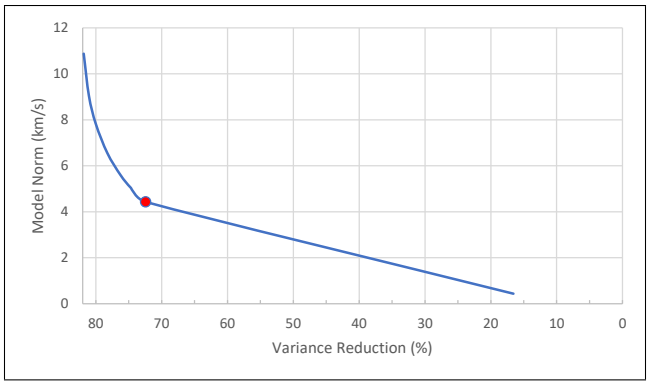

Figure 4.13: V_p trade-off curve between model norm and variance reduction for AK135 as a starting model. The red circle is the perceived corner.

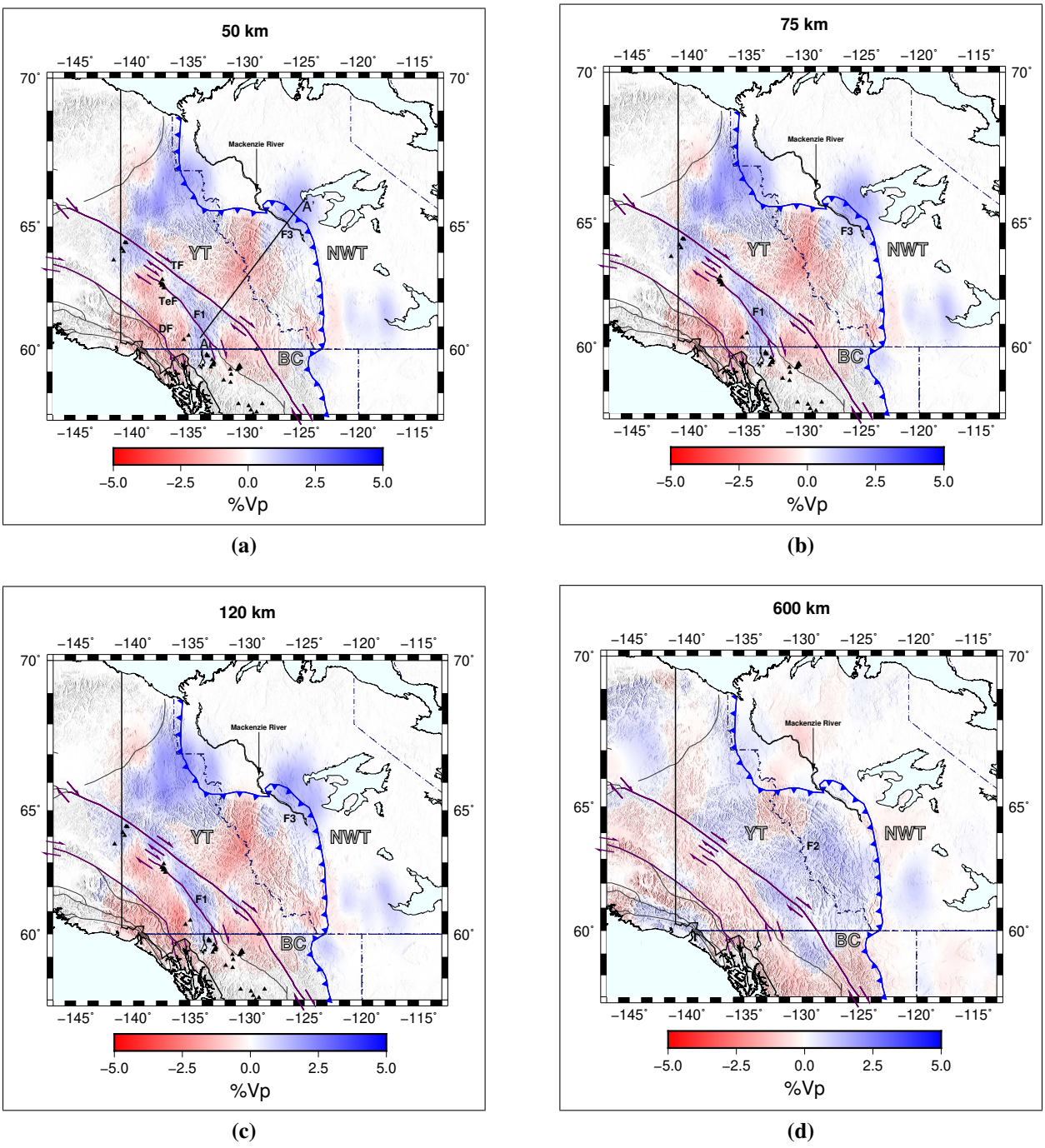

Figure 4.14: V_p perturbations with respect to 1-D AK135 global model. F1, F2 and F3 are the three notable high velocity anomalies in the region. TF=Tintina Fault, TeF=Teslin Fault, DF=Denali Fault, YT=Yukon Territory, NWT=Northwest Territories, BC=British Columbia.

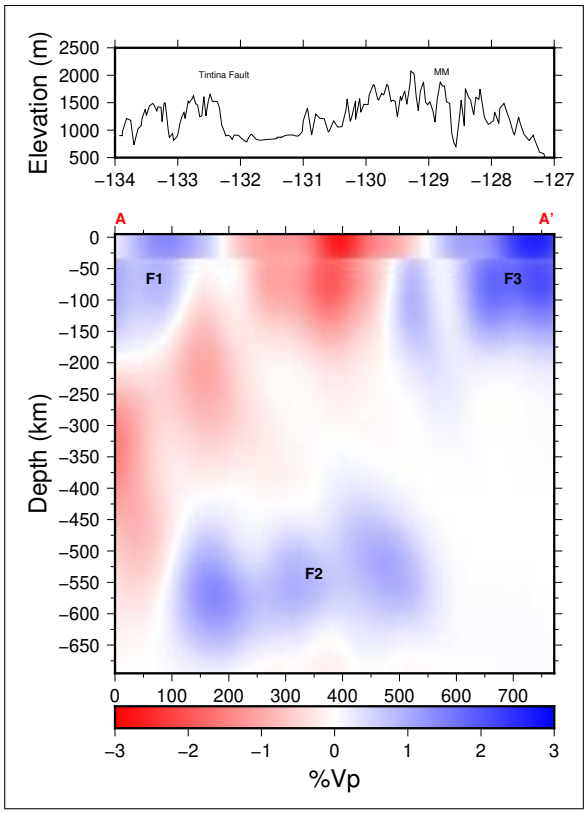

Figure 4.15: Cross section along the AA' line (Figure 4.14a) showing percent V_p perturbations. x-axis shows distance from point A in kilometers. F1, F2, and F3 are the high velocity anomalies. Spatially, F1 and F3 correspond to the locations of the Yukon-Tanana terrane and the Canadian craton, respectively. F2 is interpreted as the delaminated lithosphere. The middle interface is at 34 km.

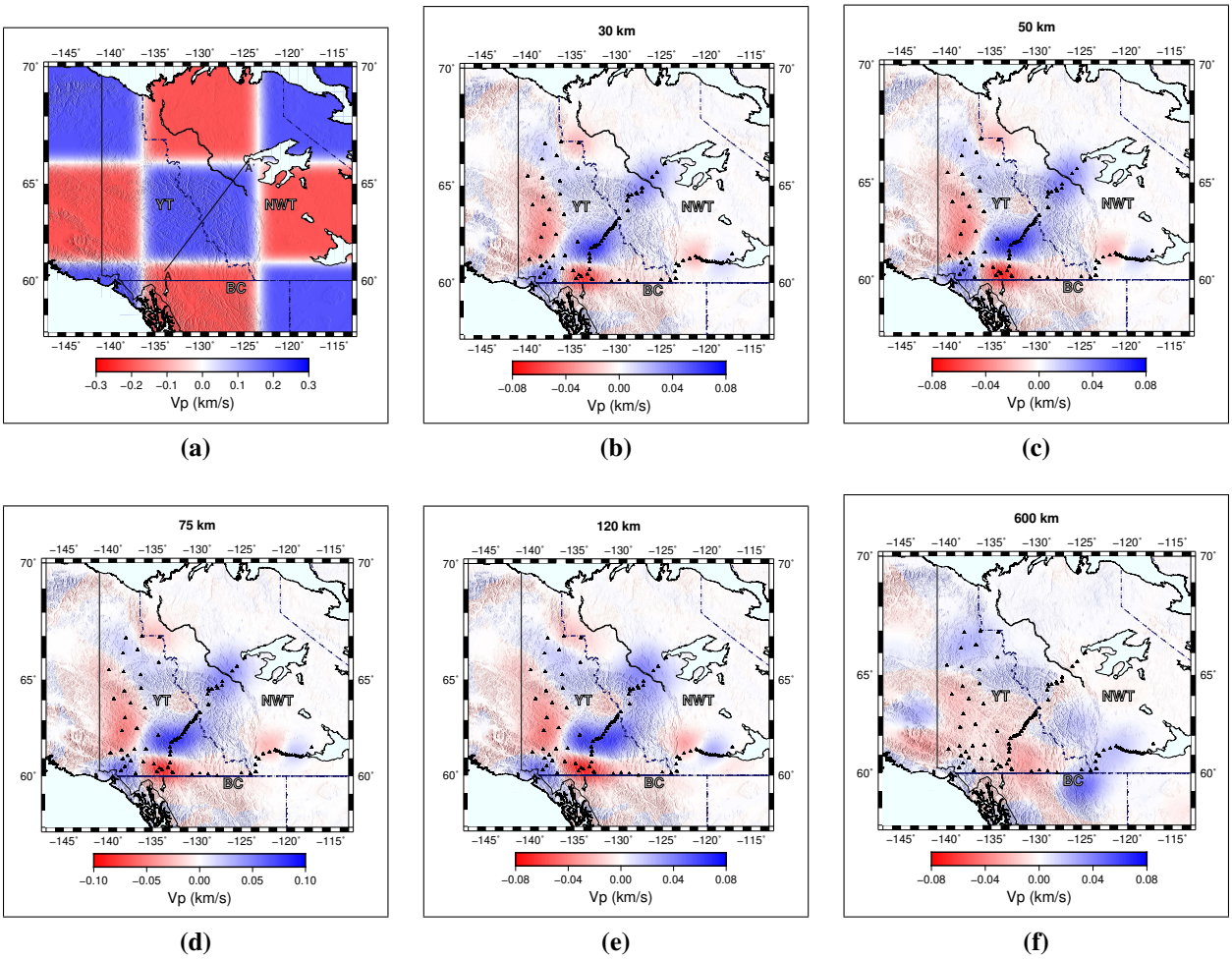

Figure 4.16: Depth slices of V_p input checkerboard and recovered checkerboard at different depths. The same value of damping (75) as that in the case of the real inversion was used here. Black triangles are all the stations in the model region. Note the change in color scale for the 600 km depth slice.

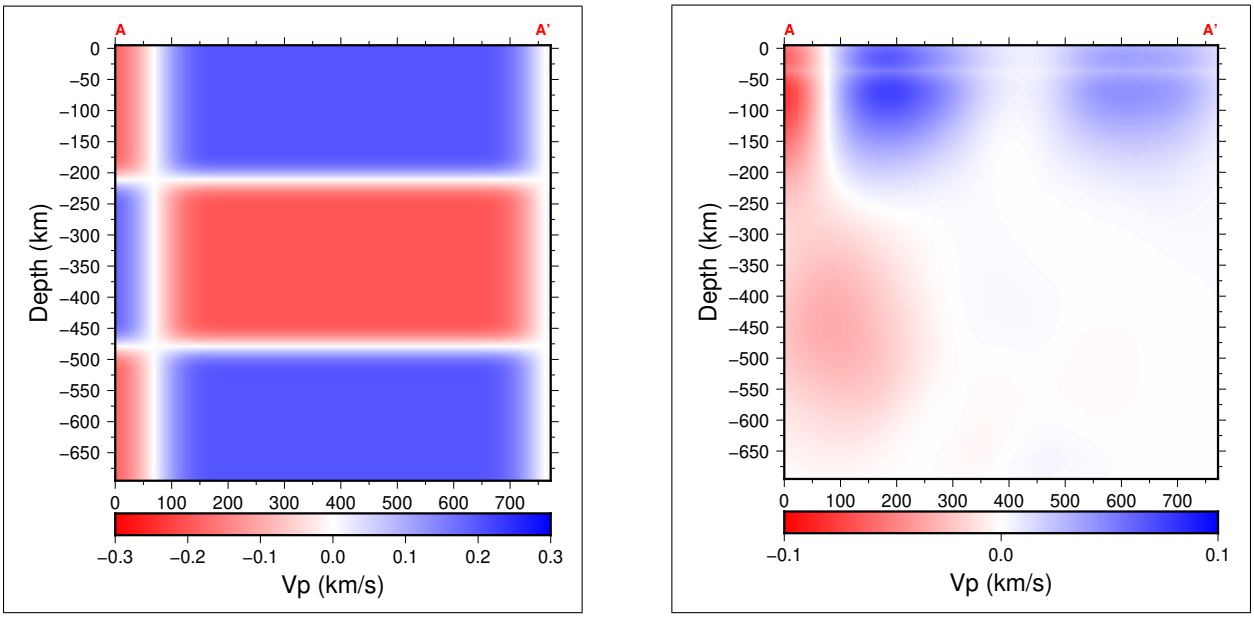

(a) **(b)**

Figure 4.17: Cross section along the AA' line (Figure 4.16a) showing V_p input checkerboard and recovered checkerboard. The middle interface was at 34 km.

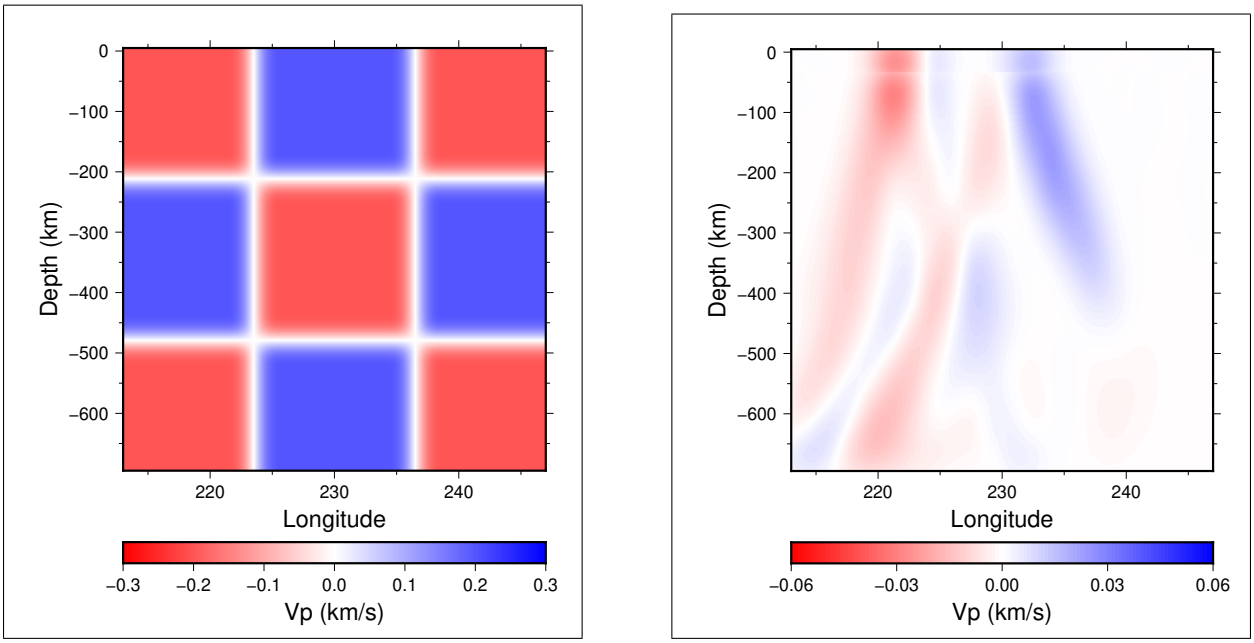

(a) **(b)**

Figure 4.18: East-West cross section along the 60°N latitude showing the V_p checkerboard recovery. Low station density has caused the lack of recovered anomalies east of 237E longitude.

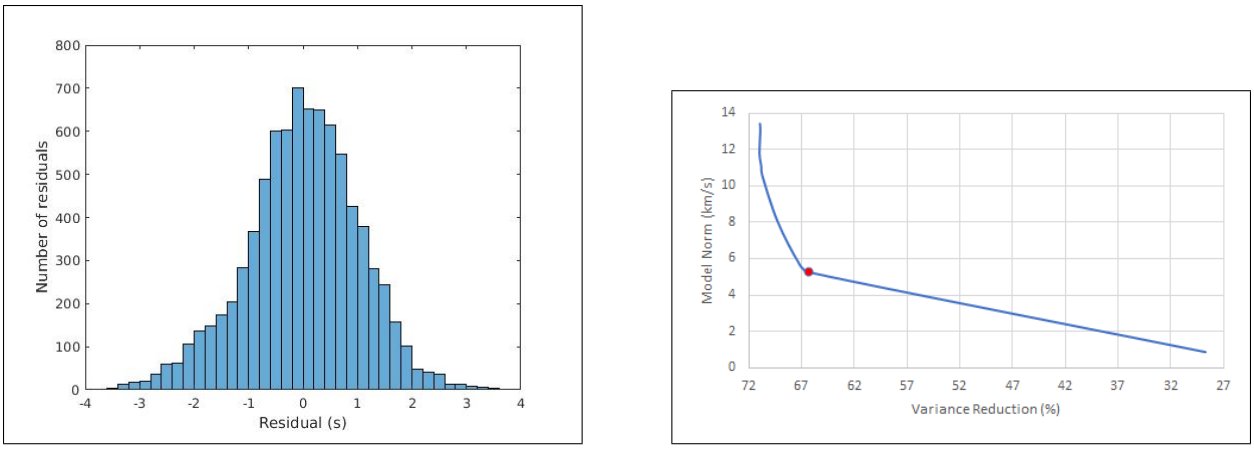

(a) **(b)**

Figure 4.19: (a) Histogram of all 8250 relative S wave residuals used in this study and (b) V_s trade-off curve between model norm and variance reduction for AK135 as the starting model. The red circle is the corner of the curve.

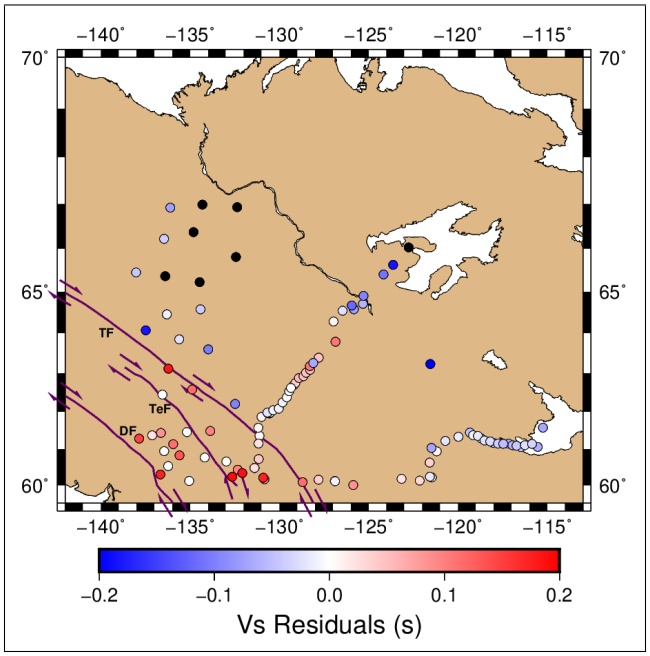

Figure 4.20: Plot of mean V_s residual at each station in the NCC. TF=Tintina fault, TeF=Teslin fault, DF=Denali fault.

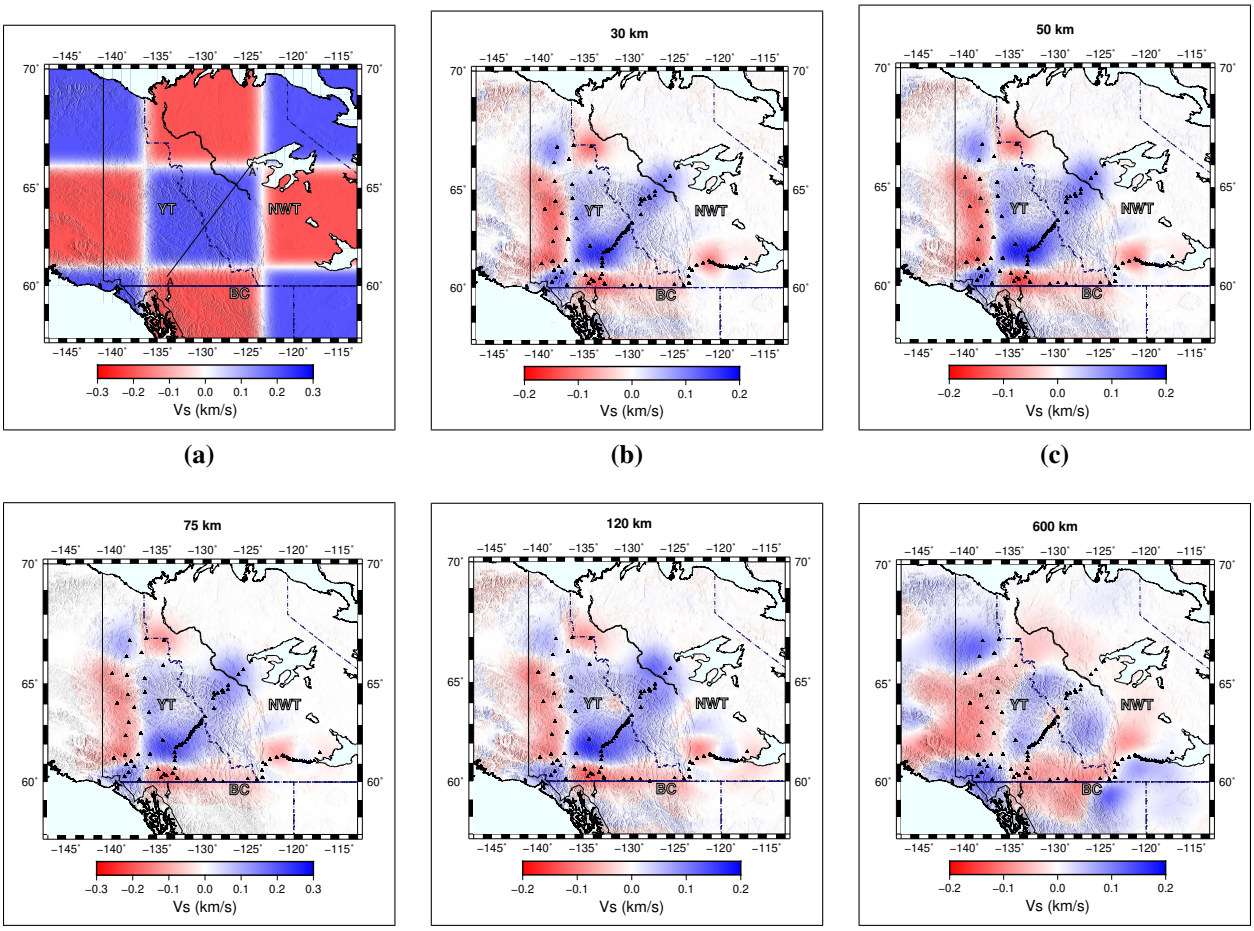

Figure 4.21: Depth slices of V_s input checkerboard and recovered checkerboard at different depths. Black triangles are all the stations in the model region. Note the change in scale for the 600 km depth slice.

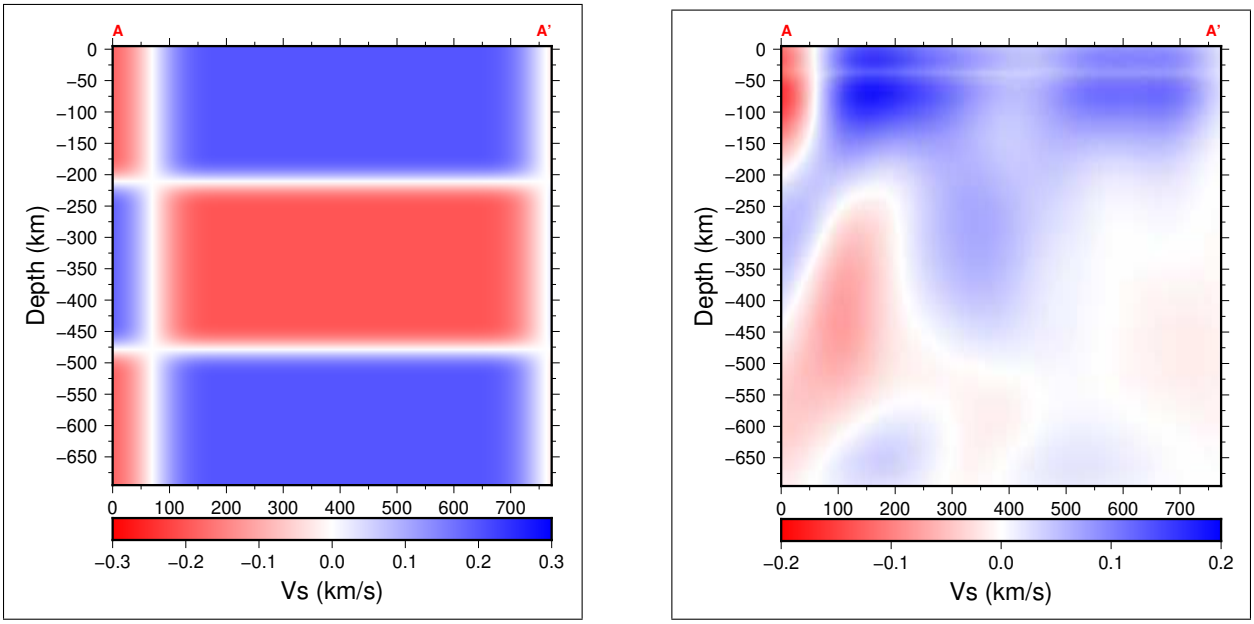

(a) **(b)**

Figure 4.22: Cross section along the AA' line (Figure 4.21a) showing V_s input checkerboard and recovered checkerboard. The middle interface was at 34 km.

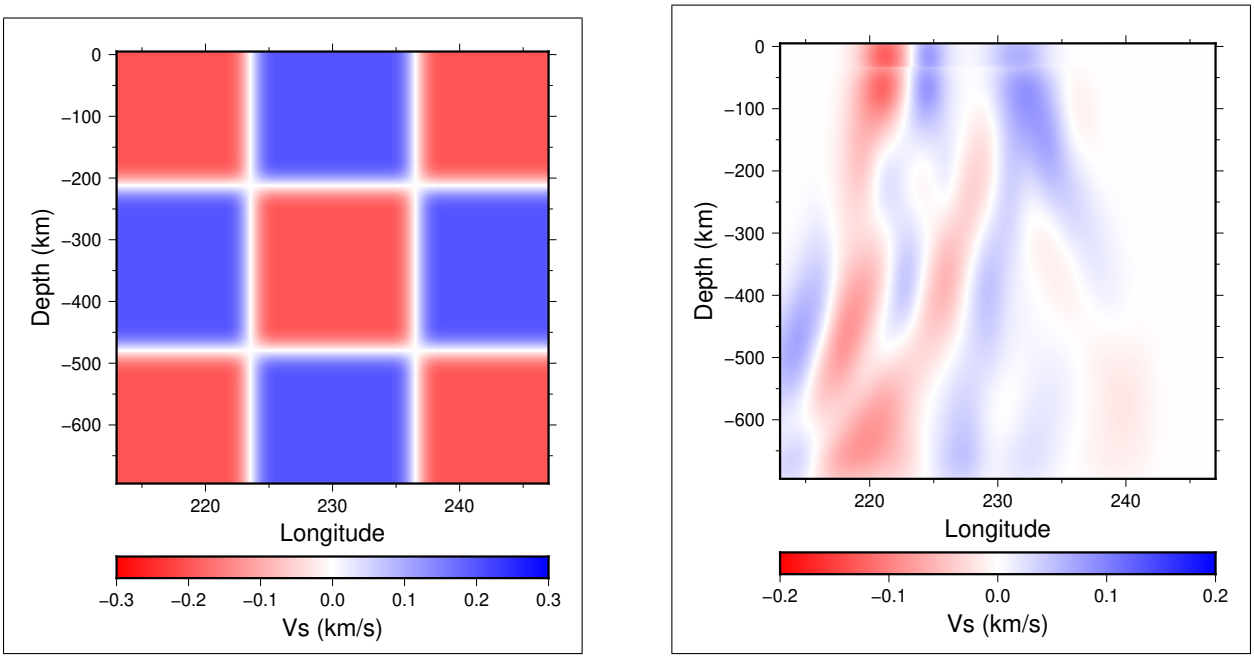

(a) **(b)**

Figure 4.23: East-West cross section along the 60°N latitude showing the V_s checkerboard recovery. Low station density has caused the lack of recovered anomalies east of 237E longitude.

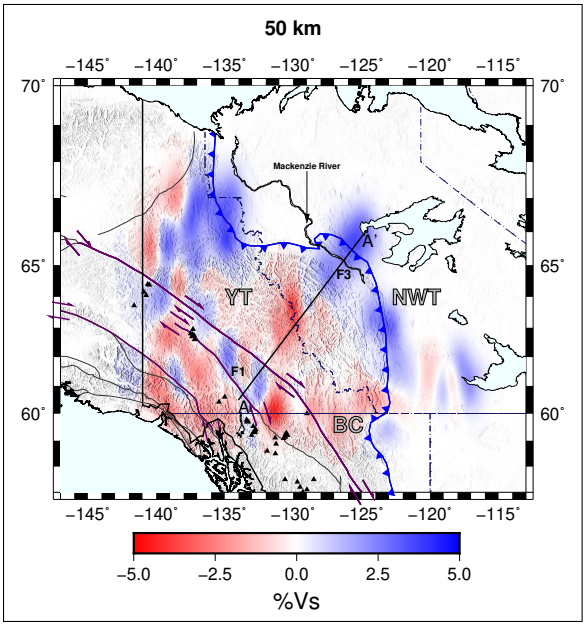

(a)

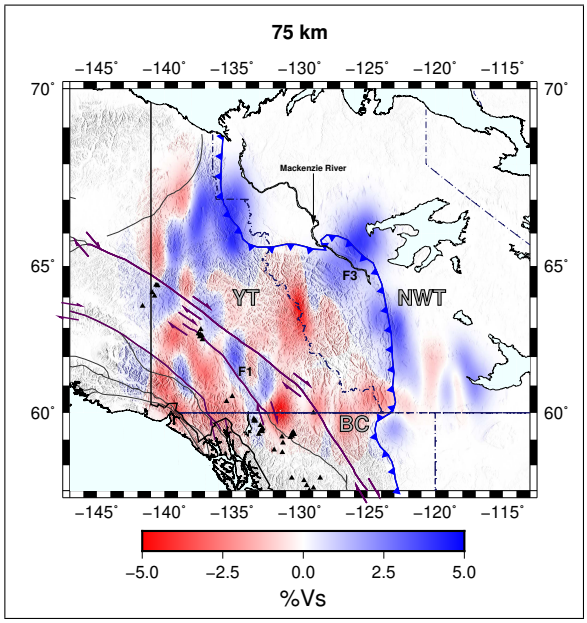

(b)

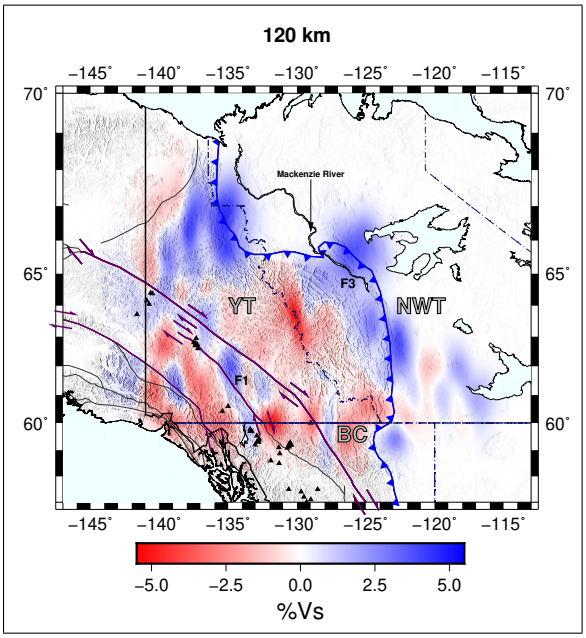

(c)

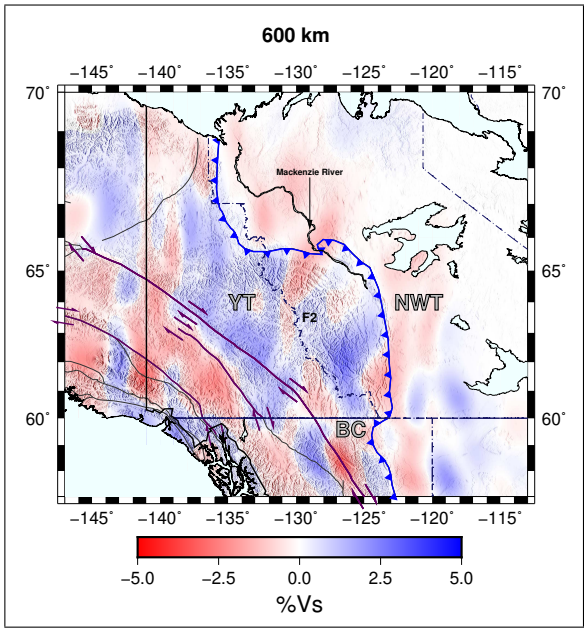

(d)

Figure 4.24: Depth slices showing V_s perturbations with respect to AK135. F1, F2, and F3 are the same anomalies as before and black triangles are the locations of volcanics. TF=Tintina Fault, TeF= Teslin Fault, DF= Denali Fault, YT=Yukon Territory, NWT=Northwest Territories, BC=British Columbia

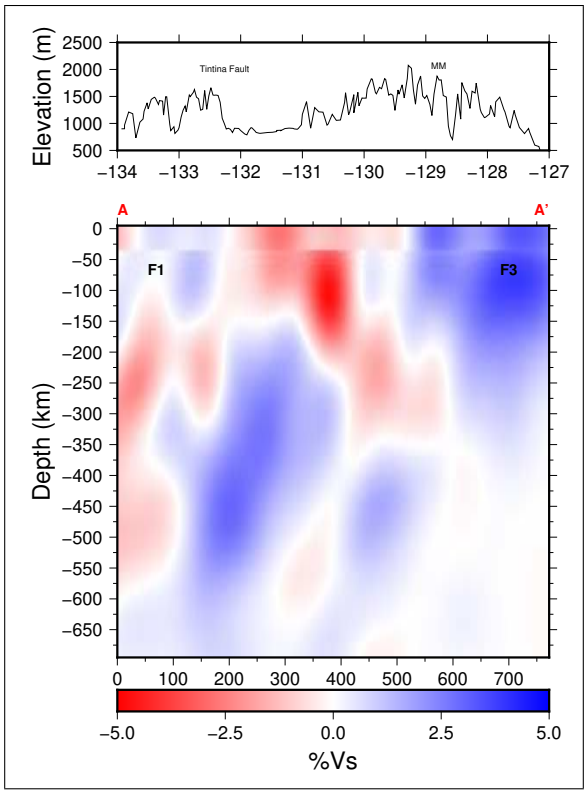

Figure 4.25: Cross section along the AA' line (Figure 4.14a) showing percent V_s perturbations with respect to AK135. x-axis shows distance from point A in kilometers. F1, and F3 are the same high velocity anomalies. F2 anomaly at 600 km is smeared vertically and hence not labeled.

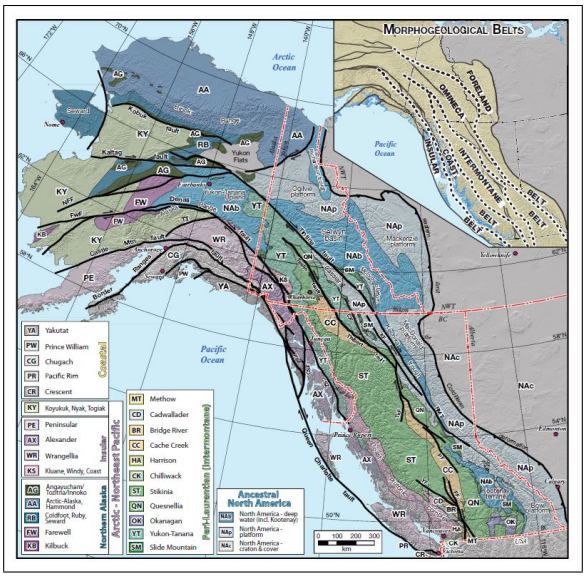

Figure 4.26: Map of the different morphologic belts in the NCC (Nelson et al. [2013]).

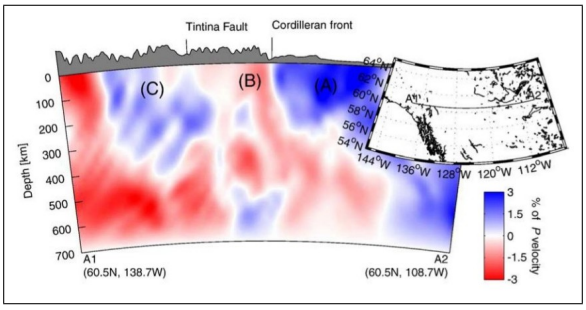

Figure 4.27: An east-west cross section along the southern border of the NCC. The cross section line is seen in the inset map. (A)=Canadian craton, (B)=low velocity Cordillera, (C)=high velocity anomaly under the Tintina Fault (Mercier et al. [2009])

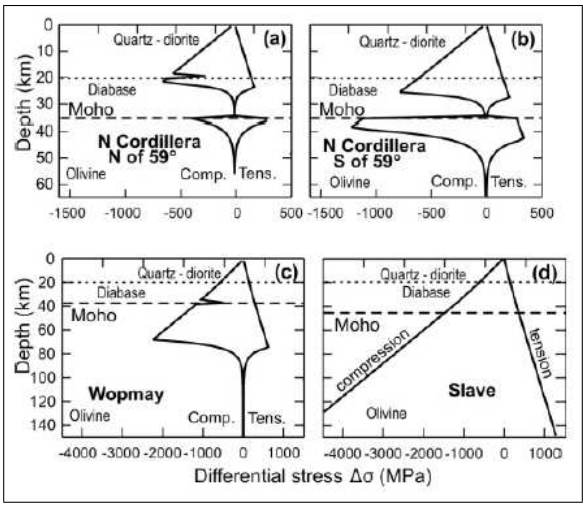

Figure 4.28: Lithospheric strength profiles from Hyndman et al. [2005]. As predicted by the orogenic float hypothesis, a weak lower crust lies between a relatively strong upper crust and a weak upper mantle in the NCC. Notice the change in scale for differential stress between the Cordillera and craton.

References

Aster, R., Borchers, B., and Thurber, C. (2011). *Parameter Estimation and Inverse Problems*. Academic Press.

Audet, P., Currie, C., Schaeffer, A., and Hill, A. (2019). Seismic evidence for lithospheric thinning and heat in the northern canadian cordillera. *Geophysical Research Letters*, 46:4249–4257.

Audet, P., Jellinek, M., and Hideharu, U. (2007). Mechanical controls on the deformation of continents at convergent margins. *Earth and Planetary Science Letters*, 264:151–166.

Baker, M., Heath, D., Schutt, D., Aster, R., Cubley, J., and Freymueller, J. (2019). The mackenzie mountains earthscope project: Studying active deformation in the northern north american cordillera from margin to craton. *Seismological Research Letters*.

Bao, X., Eaton, D., and Guest, B. (2014). Plateau uplift in western canada caused by lithospheric delamination along a craton edge. *Nature Geoscience*, 7:830–833.

Cecile, M. P., Morrow, D. W., and Williams, G. K. (1997). Early paleozoic (cambrian to early devonian) tectonic framework, canadian cordillera. *Bulletin of Canadian Petroleum Geology*, 45:54–74.

Cook, F. A., M, C. R., B, S. D., van der Velden, A. J., Hall, K. W., Erdmer, P., and Evenchick, C. A. (2004). Precambrian crust beneath the mesozoic northern canadian cordillera discovered by lithoprobe seismic reflection profiling. *Tectonics*.

Dziewonski, A. M. and Anderson, D. L. (1981). Preliminary reference earth model. *Physics of the Earth and Planetary Interiors*, 25:297–356.

Edwards, B. R. and Russell, J. K. (2000). Distribution, nature, and origin of neogene-quaternary magmatism in the northern cordilleran volcanic province, canada. *GSA Bulletin*, 112:1280–1295.

Enkelmann, E., Finzel, E., and Arkle, J. (2019). Deformation at the eastern margin of the northern canadian cordillera: Potentially related to opening of the north atlantic. *Terra Nova*, pages 151–156.

Finzel, E. S., Flesch, L. M., Ridgeway, K. D., Holt, W. E., and Ghosh, A. (2015). Surface motions and intraplate continental deformation in alaska driven by mantle flow. *Geophysical Research Letters*, 42:4350–4358.

Fluck, P., Hyndman, R. D., and Lowe, C. (2003). Effective elastic thicknessteof the lithosphere in western canada. *Journal of Geophysical Research*, 108.

Gabrielse, H., Murphy, D. C., and Mortensen, J. K. (2006). Cretaceous and cenozoic dextral orogen-parallel displacements, magmatism, and paleogeography, north-central canadian cordillera. *Geological Association of Canada, Special Paper*, pages 255–276.

Gordey, S. P., Macdonald, J. D., Turner, E. C., and G, L. D. (2011). Structural geology of the central mackenzie mountains. *Geology of the Central Mackenzie Mountains of the Northern Canadian Cordillera, Sekwi Mountain (105P), Mount Eduni (106A), and the Northwestern Wrigley Lake (95M) Map Areas, Northwest Territories, NWT Special*, 1:215–250.

Hammond, W. and Humphreys, E. (2000). Upper mantle seismic wave velocity: Effects of realistic partial melt geometries. *Journal of Geophysical Research*, 105.

Hansen, V. L., Goodge, J. W., Keep, M., and Oliver, D. H. (1993). Assymetric rift interpretation of the western north american margin. *Geology*, 21:1067–1070.

Hayward, N. (2018). The 3d geophysical investigation of a middle cretaceous to paleocene regional dÃl'collement in the cordillera of northern canada and alaska. *Tectonics*, 38:307–334.

Hyndman, R. D. (2010). The consequences of canadian cordillera thermal regime in recent tectonics and elevation: a review. *Canadian Journal of Earth Sciences*, 47:621–632.

Hyndman, R. D., Fluck, P., Mazzotti, S., Lewis, T. J., Ristau, J., and Leonard, L. (2005). Current tectonics of the northern canadian cordillera. *Canadian Journal of Earth Sciences*, 42:1117–1136.

Karato, S. (1993). Importance of anelasticity in the interpretation of seismic tomography. *Geophysical Research Letters*, 20:1623–1626.

Kennett, B. L., Engdahl, E. R., and Buland, R. (1985). Constraints on seismic velocities in the earth from travel times. *Geophysical Journal International*, pages 108–124.

Leonard, L. J. (2006). Gps and seismicity constraints on the current tectonics of the northern canadian cordillera, ph.d. thesis.

Leonard, L. J., Hyndman, R. D., Mazzotti, S., Nykolaishen, L., Schmidt, M., and Hippchen, S. (2007). Current deformation in the northern canadian cordillera inferred from gps measurements. *Journal of Geophysical Research*.

Leonard, L. J., Mazzotti, S., and Hyndman, R. D. (2008). Deformation rates estimated from earthquakes in the northern cordillera of canada and eastern alaska. *Journal of Geophysical Research*.

Lewis, T. J., Hyndman, R. D., and Fluck, P. (2003). Heat flow, heat generation, and crustal temperatures in the northern canadian cordillera: Thermal control of tectonics. *Journal of Geophysical Research*, 108.

Marechal, A., Mazzotti, S., L, E. J., Freymueller, J. T., and Schmidt, M. (2015). Indentor-corner tectonics in the yakutat-st. elias collision constrained by gps. *Journal of Geophysical Research: Solid Earth*, 120.

Mazzotti, S. and Hyndman, R. D. (2002). Yakutat collision and strain transfer across the northern canadian cordillera. *Geological Society of America*, 30:495–498.

McLellan, M., Schaeffer, A., and Pascal, A. (2018). Structure and fabric of the crust and uppermost mantle in the northern canadian cordillera from rayleigh-wave tomography. *Tectonophysics*, 724-725:28–41.

Mercier, J. P., Bostock, M. G., Cassidy, J. F., Dueker, K., Gaherty, J. B., Garnero, E. J., Revenaugh, J., and Zandt, G. (2009). Body-wave tomography of western canada. *Tectonophysics*, pages 480–492.

Monger, J. and Price, R. (2002). The canadian cordillera: Geology and tectonic evolution. *Canadian Society of Exploration Geophysicists*, pages 17–36.

Nelson, J., Colpron, M., and Israel, S. (2013). The cordillera of british columbia, yukon, and alaska: Tectonics and metallogeny. *Society of Economic Geologists*, 17:53–109.

Nolet, G. (1987). *Seismic Tomography*. D. Reidel Publishing Company.

Oldow, J., Bally, A., and Lallemant, H. (1990). Transpression, orogenic float, and lithospheric balance. *Geology*, 18:991–994.

Owens, T. J., Crotwell, H. P., Grover, C., and Oliver-Paul, P. (2004). Sod: Standing order for data. *Seismological Research Letters*, 75:515–520.

Page, R. A., Biswas, N. N., Lahr, J. C., and Pulpan, H. (1991). Seismicity of continental alaska. *Neotectonics of North America, Decade Map, vol. 1*, pages 47–68.

Plafker, G., Moore, J. C., and Winkler, G. R. (1994). Geology of the southern alaska margin. *The Geology of Alaska*, G-1:389–449.

Powell, J., Schneider, D., Stockli, D., and Fallas, K. (2016). Zircon (uâĂŘth)/hhe thermochronology of neoproterozoic strata from the mackenzie mountains, canada; implications for the phanerozoic exhumation and deformation history of the northern canadian cordillera. *Tectonics*, 35:663–689.

Rawlinson, N., Hauser, J., and Sambridge, M. (2007). Seismic ray tracing and wavefront tracking in laterally heterogeneous media. *Advances in Geophysics*, 49:203–267.

Rawlinson, N. and Sambridge, M. (2005). The fast marching method: an effective tool for tomographic imaging and tracking multiple phases in complex layered media. *Exploration Geophysics*, pages 341–350.

Schaeffer, A. J. and Lebedev, S. (2014). Imaging the north american continent using waveform inversion of global and usarray data. *Earth and Planetary Science Letters*, pages 26–41.

Sethian, J. A. (1996). Fast marching methods and level set methods for propagating interfaces.

Stein, S. and Wysession, M. (2003). *An Introduction to Seismology, Earthquakes and Earth Structure*. Blackwell Publishing.

Thorkelson, D., Madsen, J., and Sluggett, C. (2011). Mantle flow through the northern cordilleran slab window revealed by volcanic geochemistry. *Geology*, 39:267–270.

Thorkelson, D. and Taylor, R. (1989). Cordilleran slab windows. *Geology*, pages 833–836.

VanDecar, J. C. and Crosson, R. S. (1990). Determination of teleseismic relative phase arrival times using multi-channel cross-correlation and least squares. *Bulletin of the Seismological Society of America*, 80:150–169.

Wei, W., Jiandong, X., Dapeng, Z., and Yaolin, S. (2012). East asia mantle tomography: New insight into plate subduction and intraplate volcanism. *Journal of Asian Earth Sciences*, 60:88–103.